Resonances from meson-meson scattering in $U(3)$ χPT

Zhi-Hui Guo[1,2*] and J. A. Oller[2†]

[1] *Department of Physics. Hebei Normal University. 050016 Shijiazhuang. China*
[2] *Departamento de Física. Universidad de Murcia. E-30071 Murcia. Spain*

Abstract

In this work, the complete one loop calculation of meson-meson scattering amplitudes within $U(3)\otimes U(3)$ chiral perturbation theory with explicit resonance states is carried out for the first time. Partial waves are unitarized from the perturbative calculation employing a non-perturbative approach based on the N/D method. Once experimental data are reproduced in a satisfactory way we then study the resonance properties, such as the pole positions, corresponding residues and their N_C behaviors. The resulting N_C dependence is the first one in the literature that takes into account the fact that the η_1 becomes the ninth Goldstone boson in the chiral limit for large N_C. Within this scheme the vector resonances studied, $\rho(770)$, $K^*(892)$ and $\phi(1020)$, follow an N_C trajectory in agreement with their standard $\bar{q}q$ interpretation. The scalars $f_0(1370)$, $a_0(1450)$ and $K^*(1430)$ also have for large N_C a $\bar{q}q$ pole position trajectory and all of them tend to a bare octet of scalar resonances around 1.4 GeV. The $f_0(980)$ tends asymptotically to the bare pole position of a singlet scalar resonance around 1 GeV. The σ, κ and $a_0(980)$ scalar resonances have a very different N_C behavior and move far away in the complex plane for large N_C.

1 Introduction

A completely reliable theory to describe the physics in the intermediate energy region (resonance region) of QCD is still missing nowadays, since neither the low energy effective theory of QCD, namely chiral perturbation theory (χPT) nor perturbative QCD is valid in this region. The appearance of very broad resonances, such as σ and κ [1], makes the discussion even more difficult and thus posts a great challenge for theorists. Several attempts have been done to address the question by implementing non-perturbative methods inspired in the S-matrix theory [2, 3, 4], typically on the χPT results. One has approaches like the Inverse Amplitude Method (IAM) [5, 6, 7, 8] to establish the unitarized amplitudes, others are based on the N/D equations [9, 10, 11, 12, 13], Roy equations [14, 15, 16], or on building specific dispersion relations for the scattering amplitudes [17, 18], etc. Although the different approaches determine values for the pole positions of the broad resonances σ and κ in good agreement between each other, their nature is still a controversial subject. One way to get insight into them is to track the N_C trajectories of resonance poles in the complex plane. All the previous works along this research line [19, 20, 21, 22, 23, 24] are performed within $SU(3)$ or $SU(2)$ χPT [25]. In the former case the degrees of freedom correspond to the lightest octet of pseudoscalar mesons, pions π, kaons K and the isoscalar η_8, while the singlet pseudoscalar η_1 is considered as a heavy field buried in the chiral counterterms. In the case of $SU(2)$ χPT only pions are taken as degrees of freedom.

*guo@um.es
†oller@um.es

$U(3)\otimes U(3)$ chiral symmetry in QCD is broken because of quantum effects that violate the conservation of the singlet axial vector current by the $U_A(1)$ anomaly [26, 27, 28]. As a result the pseudoscalar η' is not a pseudo-Goldstone boson [29]. Nevertheless, from the large N_C QCD point of view, the quark loop responsible for the $U_A(1)$ anomaly [26] is $1/N_C$ suppressed, thus indicating that the η' becomes the ninth pseudo-Goldstone boson in the large N_C limit [30]. Hence it is necessary to include the η' meson as a dynamical degree of freedom if one attempts to discuss the N_C trajectories of various resonances. This important fact was lacking in previous studies and is one of the main motivations of our current work.

Thanks to the large N_C QCD, the singlet η_1 field can be conveniently incorporated into the effective field theory by enlarging the number of degrees of freedom of the theory from the octet of pseudo-Goldstone bosons to the nonet, which is usually called $U(3)$ χPT [31]. Compared with $SU(3)$ χPT, a novel ingredient in $U(3)$ χPT is the η_1 mass term from the $U_A(1)$ anomaly, which has nothing to do with the current quark masses. The appearance of this new scale in χPT could totally breakdown the well celebrated chiral power counting. The introduction of the $1/N_C$ expansion in $U(3)$ χPT fixes the problem, since the singlet mass M_0 behaves as $\mathcal{O}(1/N_C)$ in the large N_C limit. Thus, in $U(3)$ χPT there are three expansion parameters: momentum, quark masses and $1/N_C$, giving rise to a joint triple expansion $\delta \sim p^2 \sim m_q \sim 1/N_C$. However, one should bear in mind that the value of the singlet mass M_0, around 950 MeV, mainly determined from the masses of the physical states η and η', is by no means a small quantity. In connection with this problem Ref.[32] used the infrared regularization method (IR), which is proposed to cure chiral violating terms from loop corrections in baryon chiral perturbation theory in the low energy region [33, 34], to investigate the η' physics within $U(3)$ χPT. In IR the basic one loop scalar integral is divided into the infrared singular and regular parts. The regular part is not considered in IR because its effects are absorbed into the low energy constants of the theory. One only needs to consider the infrared singular part. However, contrary to baryon chiral perturbation theory, nothing prevents the appearance of large η' masses in the vertices from derivatives acting on the external η' fields, while this is not an issue in baryon chiral perturbation theory because of baryon number conservation. By the same token in meson χPT the total energy squared in the center of mass frame (CM) is not restricted to be around one, two, etc η' masses, which could indeed spoil the validity of a loop calculation within IR. Although there are some special processes, such as $\eta' \to \eta\pi\pi$ [32], which happens to be covered by the constrained energy region of IR, in general one can not naively apply IR in the pure meson sector.

In the present discussion, we employ standard dimensional regularization, as in conventional $SU(3)$ χPT [25]. Then, the triple chiral expansion scheme is necessary for preserving the power counting. Investigations within $U(3)$ χPT along this line mainly focused on the construction of higher order Lagrangians [35, 36] and the tree level and one-loop calculations for $\eta - \eta'$ mixing [37, 38]. An important contribution of our work is to offer the first complete one-loop calculation in $U(3)$ χPT for meson-meson scattering, including both the loop diagrams contributing to the pseudo-Goldstone masses and decay constants, as well as the genuine ones of meson-meson scattering. Previous analyses only considered tree level amplitudes or performed partial one-loop calculations [39, 40, 41]. The $\eta' \to \eta\pi\pi$ decay was studied in detail. Ref. [32] performed a one-loop calculation within IR, and Ref. [42] undertook a two-loop calculation within the framework of non-relativistic field theory. However, in this decay the three-momenta of the pions are not small compared with their mass for some region of the kinematics. Recently, Ref. [43] discussed the same process within the triple expansion scheme by considering tree level amplitudes and part of the s-channel loops, resumming $\pi\pi$ final state interactions.

Since one of the main interests of our work is to study resonance properties, we will explicitly include bare resonance fields in the Lagrangian within the framework of resonance chiral theory [44, 45]. However, including resonances as dynamical degrees of freedom is not enough to guarantee that one can safely apply the perturbative results up to the resonance region, since the loops of pseudo-Goldstone bosons, specially

the unitarity or the s-channel loops, start to play an important role around the energy region where resonances emerge. Thus, a proper way to resum unitarity loops is crucial to study resonance properties. We use in this work the method provided in Ref. [10] to accomplish this resummation. Notice also that not all the resonances that stem in our study correspond to bare fields because new resonances come out when strong enough interactions are resummed.

The present paper is organized as follows. Section 2 is devoted to the introduction of the relevant chiral Lagrangian. The structure of the perturbative scattering amplitudes is elaborated in Section 3, which is followed by the partial wave projection and its unitarization in Section 4. The phenomenological discussion, including the fit quality and features of resonances, such as masses, widths, residues and N_C behavior, is given in detail in Section 5. We conclude in Section 6.

2 Relevant Chiral Lagrangian

The chiral Lagrangian at leading order in $U(3)$ χPT reads [31]

$$\mathcal{L}_\chi = \frac{F^2}{4}\langle u_\mu u^\mu\rangle + \frac{F^2}{4}\langle \chi_+\rangle + \frac{F^2}{3}M_0^2 \ln^2 \det u\,, \tag{1}$$

where $\langle\ldots\rangle$ denotes the trace in flavor space and the last term corresponds to the $U_A(1)$ anomaly η_1 mass term. The definitions for the chiral building blocks are

$$\begin{aligned} u_\mu &= iu^+ D_\mu U u^+\,,\\ \chi_+ &= u^+\chi u^+ + u\chi^+ u\,,\\ U &= u^2 = e^{i\frac{\sqrt{2}\Phi}{F}}\,,\\ D_\mu U &= \partial_\mu U - ir_\mu U + iUl_\mu\,,\\ \chi &= 2B(s+ip)\,, \end{aligned} \tag{2}$$

where $r_\mu\,, l_\mu\,, s\,, p$ stand for external sources and the pseudo-Goldstone bosons are collected in the matrix

$$\Phi = \begin{pmatrix} \frac{1}{\sqrt{2}}\pi^0 + \frac{1}{\sqrt{6}}\eta_8 + \frac{1}{\sqrt{3}}\eta_1 & \pi^+ & K^+ \\ \pi^- & \frac{-1}{\sqrt{2}}\pi^0 + \frac{1}{\sqrt{6}}\eta_8 + \frac{1}{\sqrt{3}}\eta_1 & K^0 \\ K^- & \bar{K}^0 & \frac{-2}{\sqrt{6}}\eta_8 + \frac{1}{\sqrt{3}}\eta_1 \end{pmatrix}. \tag{3}$$

In addition, F is the axial decay constant of the pseudo-Goldstone bosons in the chiral limit. In the same limit the parameter B is related to the quark condensate through $\langle 0|\bar{q}^i q^j|0\rangle = -F^2 B\delta^{ij}$. The explicit chiral symmetry breaking is implemented by taking the vacuum expectation values of the scalar external source field $s = \mathrm{Diag}(m_u, m_d, m_s)$, with m_q the light quark masses. Throughout we always work in the isospin limit, i.e. taking $m_u = m_d$.

We follow the framework in Ref.[44] to include bare resonance fields, where the interaction terms of pseudo-Goldstone bosons and resonances are invariant under chiral symmetry [46] and the discrete symmetries of charge conjugation C and parity P. Due to the presence of heavy resonance states, the momentum expansion is not valid any more in this theory. Nevertheless the $1/N_C$ expansion provides another guided principle to construct the Lagrangian. The generic N_C leading structure of the interacting operator in resonance chiral theory has only one flavor trace and in a schematic way can be written as

$$\mathcal{O}_i \sim \langle\, R_1 R_2 \ldots R_j\, \chi^{(n)}\,\rangle\,, \tag{4}$$

where $\chi^{(n)}$ denotes the chiral building block with chiral order $\mathcal{O}(p^n)$, that only incorporates the pseudo-Goldstone bosons and the external source fields, and R_i stands for the resonance fields. Although in the resonance chiral theory the interacting terms with higher chiral orders ($n \geq 4$) are not suppressed in general, many of them are absent if one invokes the short distance constraints from QCD in large N_C [45] and does not allow fine tuning between different operators [47]. To be practical in the phenomenological discussion we restrict ourselves by including the full set of operators with $n \leq 2$. Concerning the number of resonance states in the interacting vertices, the most relevant ones in meson-meson scattering consist of one single resonance field.

In regards to the operators attached only to the interactions between the pseudo-Goldstone bosons beyond leading order, it is commonly believed that they encode the high energy dynamics of the underlying theory, which could be represented by the heavier states, such as resonances. It has been shown that at $\mathcal{O}(p^4)$ in $SU(3)$ χPT the low energy constants (LECs) are saturated in good approximation by the lowest multiplet of resonances and thus no additional pieces of LECs seem to be typically needed in the theory [44, 45].

In the present work, we exploit this assumption on the saturation of the LECs by the lightest resonances, so that, instead of local chiral terms contributing to meson-meson scattering we take the tree level exchanges of the scalar and vector resonances. In this way we keep all local contributions to meson-meson scattering up to and including $\mathcal{O}(\delta^3)$, while also generating higher order ones. We also calculate in addition the one-loop contributions that count one order higher in δ.

The relevant resonance operators for the interactions with the pseudo-Goldstone bosons read [44]

$$\begin{aligned}\mathcal{L}_S &= c_d\langle\, S_8 u_\mu u^\mu \,\rangle + c_m\langle\, S_8\chi_+ \,\rangle + \widetilde{c}_d S_1\langle\, u_\mu u^\mu \,\rangle + \widetilde{c}_m S_1\langle\, \chi_+ \,\rangle \\ &\quad + \hat{c}_d\langle\, S_9 u_\mu \,\rangle\langle\, u_\mu \,\rangle + \hat{c}_m S_1 \ln^2 \det u\,, \end{aligned} \tag{5}$$

$$\mathcal{L}_V = \frac{iG_V}{2\sqrt{2}}\langle V_{\mu\nu}[u^\mu, u^\nu]\rangle\,, \tag{6}$$

where the resonance states are collected in the building block $R = S, V$,

$$\begin{aligned} S_1 &= \sigma_1\,, \\ S_8 &= \begin{pmatrix} \frac{a_0^0}{\sqrt{2}} + \frac{\sigma_8}{\sqrt{6}} & a_0^+ & \kappa^+ \\ a_0^- & -\frac{a_0^0}{\sqrt{2}} + \frac{\sigma_8}{\sqrt{6}} & \kappa^0 \\ \kappa^- & \bar{\kappa}^0 & -\frac{2\sigma_8}{\sqrt{6}} \end{pmatrix}, \\ S_9 &= S_8 + \frac{1}{\sqrt{3}} S_1\,, \\ V_{\mu\nu} &= \begin{pmatrix} \frac{\rho_0}{\sqrt{2}} + \frac{1}{\sqrt{6}}\omega_8 + \frac{1}{\sqrt{3}}\omega_1 & \rho^+ & K^{*+} \\ \rho^- & -\frac{\rho_0}{\sqrt{2}} + \frac{1}{\sqrt{6}}\omega_8 + \frac{1}{\sqrt{3}}\omega_1 & K^{*0} \\ K^{*-} & \bar{K}^{*0} & -\frac{2}{\sqrt{6}}\omega_8 + \frac{1}{\sqrt{3}}\omega_1 \end{pmatrix}_{\mu\nu}. \end{aligned} \tag{7}$$

The corresponding kinetic terms for resonance states read [44]

$$\begin{aligned}\mathcal{L}^V_{\rm kin} &= -\frac{1}{2}\langle\, \nabla^\lambda V_{\lambda\mu}\nabla_\nu V^{\nu\mu} - \frac{1}{2}M_V^2 V_{\mu\nu}V^{\mu\nu}\,\rangle\,, \\ \mathcal{L}^S_{\rm kin} &= \frac{1}{2}\langle\, \nabla^\mu S_8 \nabla_\mu S_8 - M_{S_8}^2 S_8^2\,\rangle + \frac{1}{2}\big(\partial^\mu S_1 \partial_\mu S_1 - M_{S_1}^2 S_1^2\big)\,, \end{aligned} \tag{8}$$

where

$$\begin{aligned}\nabla_\mu R &= \partial_\mu R + [\Gamma_\mu, R]\,, \quad R = V, S,\\ \Gamma_\mu &= \frac{1}{2}\Big[u^\dagger(\partial_\mu - i\, r_\mu)u + u(\partial_\mu - i\, l_\mu)u^\dagger\Big]\,.\end{aligned} \tag{9}$$

Compared with Ref. [44] two additional $1/N_C$ suppressed operators appear in $\mathcal{L}_S$ due to the inclusion of the singlet η_1. These are the monomials proportional to $\hat{c}_d$ and $\hat{c}_m$ in Eq. (5). From the exchange of the scalar resonances these terms give rise to tree-level meson-meson contributions that are higher order, at least $\mathcal{O}(\delta^4)$. In addition, these new operators mainly contribute to processes involving the η' meson[1] and since we deal with experimental data related to π, K and η in the present discussion, as shown explicitly below, the states with η' only enter through an indirect way. So their effects are rather tiny in the current discussion and we discard these two new terms throughout. We have checked that if included our results barely change. For the remaining parameters of scalar resonances, instead of imposing the large N_C relations to the parameters of octet and singlet, such as $\widetilde{c}_{d,m} = c_{d,m}/\sqrt{3}$ and $M_{\sigma_1} = M_{\sigma_8}$ [44], we free them in our discussion. In this way, we consider effects beyond leading order of $1/N_C$ in the scalar resonance Lagrangian implicitly.

The antisymmetric tensor formalism is used to describe the vector resonance since, as it is demonstrated in Ref.[45], only in this way one does not need to include extra terms in the pseudo-Goldstone Lagrangian to fulfill the QCD short distance constraints. For the vector resonances ω and ϕ, we assume ideal mixing throughout

$$\omega_1 = \sqrt{\frac{2}{3}}\omega - \sqrt{\frac{1}{3}}\phi\,, \qquad \omega_8 = \sqrt{\frac{2}{3}}\phi + \sqrt{\frac{1}{3}}\omega\,, \tag{10}$$

and we do not include any $1/N_C$ suppressed operators in this respect. Nonetheless, we employ different bare masses for the $\rho(770)$ and $K^*(892)$ in order to obtain a good fit to data.

Before finishing this section, we introduce the last pieces of the chiral Lagrangian involving only pseudo-Goldstone bosons at $\mathcal{O}(\delta)$ [36]

$$\begin{aligned}\mathcal{L}_\Lambda &= \Lambda_1 \frac{F^2}{12} D_\mu\psi D^\mu\psi - i\Lambda_2 \frac{F^2}{12}\langle\, U^+\chi - \chi^+ U\,\rangle\psi\ ,\\ \psi &= -i\ln\det U\ ,\\ D_\mu\psi &= \partial_\mu\psi - 2\langle a_\mu\rangle\ ,\end{aligned} \tag{11}$$

with $a_\mu = (r_\mu - l_\mu)/2$. The inclusion of such operators does not improve our fits to data indeed. However, we take into account the monomial proportional to Λ_2 to bring our prediction for the masses of η and η' at their physical values [1]. This is necessary in the present work, since in the fit all of the pseudo-Goldstone masses have their physical values, while we need to use our prediction for the masses when we discuss the N_C dependence of our results, in particular the movement of resonance poles with N_C. Thus, it is necessary to match our prediction for the masses of the pseudoscalars as a function of N_C with their physical values for $N_C = 3$. Precisely the Λ_2 term leads to an important contribution to the η and η' masses and in the triple expansion scheme its chiral order is lower than the one of chiral loops. Though this operator contributes to meson-meson scattering as well, it mainly contributes to the processes involving η' and the inclusion of this term barely affects the global fit. Unlike the Λ_2 operator the monomial proportional to Λ_1 in Eq. (11) only contributes to the masses and the scattering amplitudes

[1] The term with $\hat{c}_m$ is purely proportional to η_1^2 while that with $\hat{c}_d$ requires at least one η_1, which mainly becomes an η' because the η_1 contribution to the η is suppressed by the pseudoscalar mixing angle.

in an indirect way, i.e. through the normalization of the η' field, and its influence in the global fit is tiny. Indeed, if we include this counterterm in our fits to data the resulting fitted value tends to vanish. As a result, we do not consider any further the Λ_1 term neither in scattering nor for the $\eta - \eta'$ mixing and masses.

Finally, we want to point out that there is no double counting problem by having both the resonance Lagrangians in Eqs.(5)-(8) and the local pseudo-Goldstone operator Λ_2, since the Λ_2 term can be only generated by integrating out the excited pseudo scalar resonances, instead of the scalar and vector ones considered here.

3 Structure of the scattering amplitudes

Even in the leading order Lagrangian Eq.(1), the flavor eigenstates η_8 and η_1 are not mass eigenstates and we use the angle θ to describe the mixing of η_8 and η_1 at this order

$$\begin{aligned} \eta_8 &= c_\theta \overline{\eta} + s_\theta \overline{\eta}' \,, \\ \eta_1 &= -s_\theta \overline{\eta} + c_\theta \overline{\eta}' \,, \end{aligned} \tag{12}$$

with $c_\theta = \cos\theta$ and $s_\theta = \sin\theta$. In our notation $\overline{\eta}$ and $\overline{\eta}'$ are the fields that diagonalize the quadratic terms of the Lagrangian Eq. (1). The $\eta - \eta'$ mixing at leading order is discussed in Appendix B, Eqs. (B.5)-(B.7). The differences between $\overline{\eta}\,, \overline{\eta}'$ and the physical states $\eta\,, \eta'$ are caused by higher order operators, including loops, and can be treated perturbatively within the triple expansion scheme.

Next we calculate the contributions beyond the leading order to the scattering amplitudes in terms of the $\overline{\eta}$ and $\overline{\eta}'$ fields, while for the leading order terms to meson-meson scattering, stemming from $\mathcal{L}_\chi$ Eq. (1), one has to take care of the full $\eta - \eta'$ mixing (see below). We also point out that for the calculation of the basic amplitudes it is more reasonable to use the $\overline{\eta}$ and $\overline{\eta}'$ fields than the η_1 and η_8 ones. This is because the insertion of the leading order mixing of η_8 and η_1 does not increase the order of a diagram, as illustrated in Fig. 1 for a one-loop contribution. The leading order mixing is proportional to $m_K^2 - m_\pi^2$, and is always accompanied by the inclusion of one extra η_8 or η_1 propagator that compensates the chiral power of the vertex. As a result loop diagrams with an arbitrary number of insertions of $\eta_8 - \eta_1$ mixing vertices have the same order. On the contrary, the mixing of $\overline{\eta}\,, \overline{\eta}'$ only receives contribution from higher orders, which guarantees that diagrams with insertions from the $\overline{\eta} - \overline{\eta}'$ mixing are indeed suppressed.

Figure 1: The dot denotes the mixing of η_8 and η_1 at leading order, which is proportional to $m_K^2 - m_\pi^2$.

The calculation of the scattering amplitudes comprises the contact vertex from $\mathcal{L}_\chi$ Eq.(1), the one loop and resonance exchange graphs, as illustrated in Fig. 2. In addition, the mass and wave function renormalization terms, displayed in Fig. 3, should also be included. The latter ones only affect the tree level scattering amplitudes from Eq. (1) up to the order we attempt to calculate, as the contributions from the resonances and the loop diagrams are already beyond the leading order. The decay constants of the pseudo-Goldstone bosons, illustrated in Fig. 4, also give rise to one higher order contributions by rewriting F in terms of the physical ones in the leading order scattering amplitudes. We express the

scattering amplitudes in term of one single physical decay constant F_π throughout. The relation between F and F_π is given in Eq. (C.2).

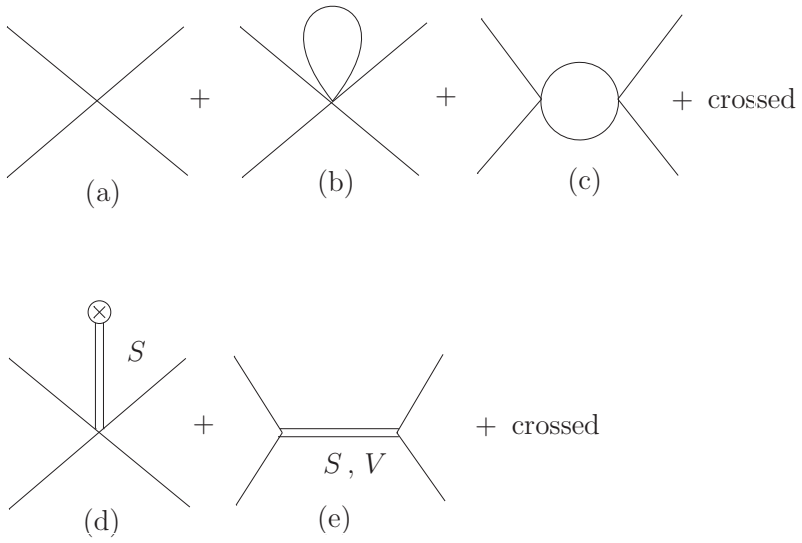

Figure 2: Relevant Feynman diagrams in the scattering amplitudes up to one-loop order. In digram (d) the coupling of the scalar resonances with the vacuum is indicated by a cross.

Figure 3: Relevant Feynman diagrams for the pseudoscalar self-energy.

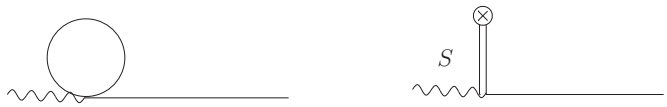

Figure 4: Relevant Feynman diagrams for the pseudoscalar decay constants. The wiggly line corresponds to the axial-vector external source.

Another subtle contribution to the scattering amplitudes is related to the $\eta - \eta'$ mixing. We recall that $\overline{\eta}\,, \overline{\eta}'$ result from the diagonalization of $\eta_8\,, \eta_1$ at leading order, Eq. (12). After including the higher order contributions from resonances and chiral loops, $\overline{\eta}\,, \overline{\eta}'$ will mix again and the physical states $\eta\,, \eta'$ can be obtained by diagonalizing $\overline{\eta}\,, \overline{\eta}'$. This extra diagonalization process contributes relevant pieces to the scattering amplitudes through the leading order results from Eq. (1). Thus it is necessary to work out the $\overline{\eta} - \overline{\eta}'$ mixing at the one loop level by calculating the diagrams in Fig. 3. However, for the already next-to-leading order contributions and higher, namely, those amplitudes obtained from the exchange of

resonances and involving loops, we do not need to distinguish between $\overline{\eta}\,,\overline{\eta}'$ and $\eta\,,\eta'$, as their differences only cause higher order effects that are beyond our current consideration.

We parameterize the higher order $\overline{\eta}-\overline{\eta}'$ mixing as

$$\begin{aligned}\mathcal{L} &= \frac{1+\delta_{\overline{\eta}}}{2}\partial_\mu\overline{\eta}\partial^\mu\overline{\eta}+\frac{1+\delta_{\overline{\eta}'}}{2}\partial_\mu\overline{\eta}'\partial^\mu\overline{\eta}'+\delta_k\,\partial_\mu\overline{\eta}\partial^\mu\overline{\eta}' \\ &\quad -\frac{m^2_{\overline{\eta}}+\delta_{m^2_{\overline{\eta}}}}{2}\overline{\eta}\,\overline{\eta}-\frac{m^2_{\overline{\eta}'}+\delta_{m^2_{\overline{\eta}'}}}{2}\overline{\eta}'\overline{\eta}'-\delta_{m^2}\,\overline{\eta}\,\overline{\eta}'\,. \end{aligned} \tag{13}$$

where $m_{\overline{\eta}}$ and $m_{\overline{\eta}'}$ defined in Eqs.(B.5) and (B.6) stand for the leading order masses of $\overline{\eta}$ and $\overline{\eta}'$ respectively, while the different δ_i, given in Eq. (B.8), contain the higher order contributions. The physical eigenstates η and η' are related with the $\overline{\eta}$ and $\overline{\eta}'$ fields by diagonalizing canonically the quadratic terms in Eq. (13) in the following way

$$\begin{pmatrix}\eta\\ \eta'\end{pmatrix}=\begin{pmatrix}\cos\theta_\delta & -\sin\theta_\delta\\ \sin\theta_\delta & \cos\theta_\delta\end{pmatrix}\begin{pmatrix}1+\frac{\delta_{\overline{\eta}}}{2} & \frac{\delta_k}{2}\\ \frac{\delta_k}{2} & 1+\frac{\delta_{\overline{\eta}'}}{2}\end{pmatrix}\begin{pmatrix}\overline{\eta}\\ \overline{\eta}'\end{pmatrix}\,. \tag{14}$$

We calculate the leading order contributions, corresponding to the diagram (a) of Fig. 2, in terms of the physical η and η' fields, so that we can directly use the physical values for the masses. Up to the order considered in our calculation for meson-meson scattering, namely, up to $\mathcal{O}(\delta^3)$ for local tree level contributions and up to $\mathcal{O}(\delta^4)$ for the one-loop graphs, we can invert Eq. (14) in a perturbative way. Then we have

$$\begin{pmatrix}\overline{\eta}\\ \overline{\eta}'\end{pmatrix}=\begin{pmatrix}1-\frac{\delta_{\overline{\eta}}}{2} & -\frac{\delta_k}{2}\\ -\frac{\delta_k}{2} & 1-\frac{\delta_{\overline{\eta}'}}{2}\end{pmatrix}\begin{pmatrix}\cos\theta_\delta & \sin\theta_\delta\\ -\sin\theta_\delta & \cos\theta_\delta\end{pmatrix}\begin{pmatrix}\eta\\ \eta'\end{pmatrix}\,, \tag{15}$$

where θ_δ is determined through

$$\tan\theta_\delta=\frac{\hat{\delta}_{m^2}}{m^2_{\eta'}-\hat{m}^2_\eta}\,, \tag{16}$$

with

$$\begin{aligned}\hat{m}^2_\eta &= m^2_{\overline{\eta}}+\delta_{m^2_{\overline{\eta}}}-m^2_{\overline{\eta}}\,\delta_{\overline{\eta}}\,,\\ \hat{m}^2_{\eta'} &= m^2_{\overline{\eta}'}+\delta_{m^2_{\overline{\eta}'}}-m^2_{\overline{\eta}'}\,\delta_{\overline{\eta}'}\,,\\ \hat{\delta}_{m^2} &= \delta_{m^2}-\frac{1}{2}\delta_k(m^2_{\overline{\eta}}+m^2_{\overline{\eta}'})\,,\\ 2m^2_{\eta'} &= \hat{m}^2_\eta+\hat{m}^2_{\eta'}+\sqrt{(\hat{m}^2_\eta-\hat{m}^2_{\eta'})^2+4\hat{\delta}^2_{m^2}}\,,\\ 2m^2_\eta &= \hat{m}^2_\eta+\hat{m}^2_{\eta'}-\sqrt{(\hat{m}^2_\eta-\hat{m}^2_{\eta'})^2+4\hat{\delta}^2_{m^2}}\,. \end{aligned} \tag{17}$$

In the previous equations θ_δ and δ_i are originated by the higher order contributions from the resonances and one loop graphs. Up to the precision we consider, it is safe to take only linear terms in the δ_i so that $\cos\theta_\delta=\sqrt{1-\sin^2\theta_\delta}\simeq 1$. From the relations between $\eta\,,\eta'$ and $\overline{\eta}\,,\overline{\eta}'$, given in Eqs.(14) and (15), there are two ways to proceed for the calculation of the physical scattering amplitudes. One method, the one that we follow, consists of writing the physical amplitudes by expressing $\overline{\eta}$ and $\overline{\eta}'$ in terms of the physical fields η and η' in Eq.(1), and then calculate the tree level amplitudes. In this way, all the masses from

the kinematics are the physical ones, since they correspond to the η and η' fields. Another method is to determine the amplitudes with η and η' by using Eq.(14) as a linear superposition of those calculated in terms of the bar fields. However, one should bear in mind that for this case the masses of $\overline{\eta}$ and $\overline{\eta}'$ from the kinematics are those of the physical η and η' fields to which they are attached.

The explicit expressions for the mass and wave function renormalization, mixing parameters entering in Eq.(13), pion decay constant, and scattering amplitudes are given in the Appendices B–D.

4 Partial wave amplitude and its unitarization

Once the perturbative amplitudes are calculated from $U(3)$ χPT, as done in the previous section, we can proceed to perform the partial wave projections of the isospin amplitudes and construct the corresponding unitarized amplitudes as well. The amplitudes T^I with well-defined isospin I from different processes are derived by assigning the following phase convention to the pseudoscalars in connection with the isospin basis states. This convention is consistent with the one taken in Eq. (3),

$$\begin{aligned}
&|\eta\rangle = |0\,0\rangle\,, \qquad |\eta'\rangle = |0\,0\rangle\,,\\
&|\pi^+\rangle = -|1\;1\rangle, \quad |\pi^-\rangle = |1\;-1\rangle, \quad |\pi^0\rangle = |1\;0\rangle\,,\\
&|K^+\rangle = -|\frac{1}{2}\;\frac{1}{2}\rangle\,, |K^0\rangle = |\frac{1}{2}\;-\frac{1}{2}\rangle\,, |\bar{K}^0\rangle = |\frac{1}{2}\;\frac{1}{2}\rangle\,, |K^-\rangle = |\frac{1}{2}\;-\frac{1}{2}\rangle\,,
\end{aligned} \tag{18}$$

where $|I\,I_3\rangle$ is a state with isospin I and third component I_3.

For $\pi\pi \to \pi\pi$ scattering there are three isospin amplitudes, $I = 0, 1, 2$. They read

$$\begin{aligned}
T^0(s,t,u) &= 3\,A(s,t,u) + A(t,s,u) + A(u,t,s)\,,\\
T^1(s,t,u) &= A(t,s,u) - A(u,t,s)\,,\\
T^2(s,t,u) &= A(t,s,u) + A(u,t,s)\,,
\end{aligned} \tag{19}$$

where $A(s,t,u)$ stands for the process $\pi^+\pi- \to \pi^0\pi^0$ and s,t,u are the standard Mandelstam variables. These equations, and other similar ones that follow, are obtained by invoking crossing symmetry [48].

For $K\pi \to K\pi$ and $\pi\pi \to K\bar{K}$, the different isospin amplitudes can also be expressed in terms of one single amplitude, again by using crossing symmetry. One then has

$$\begin{aligned}
T^{\frac{3}{2}}(s,t,u) &= T_{K^+\pi^+\to K^+\pi^+}(s,t,u)\,,\\
T^{\frac{1}{2}}(s,t,u) &= \frac{3}{2}T^{\frac{3}{2}}(u,t,s) - \frac{1}{2}T^{\frac{3}{2}}(s,t,u)\,,\\
T^0(s,t,u) &= \sqrt{\frac{3}{2}}\left[T^{\frac{3}{2}}(t,s,u) + T^{\frac{3}{2}}(u,s,t)\right],\\
T^1(s,t,u) &= T^{\frac{3}{2}}(u,s,t) - T^{\frac{3}{2}}(t,s,u)\,.
\end{aligned} \tag{20}$$

For $\pi\pi \to \eta\eta$ and $\pi\eta \to \pi\eta$, we have

$$\begin{aligned}
T^0(s,t,u) &= -\sqrt{3}\,C(s,t,u)\,,\\
T^1(s,t,u) &= C(t,s,u)\,,
\end{aligned} \tag{21}$$

with $C(s,t,u) = T_{\pi^0\pi^0\to\eta\eta}(s,t,u)$. For $\pi\pi \to \eta\eta', \eta'\eta'$ and $\pi\eta(\eta') \to \pi\eta'$, analogous formulas emerge and the only difference is that $C(s,t,u)$ is redefined accordingly to the scattering process.

The reactions $K\pi \to K\eta$ and $K\eta'$ are pure $I = 1/2$ and are given by

$$T^{\frac{1}{2}}(s,t,u) = -\sqrt{3}T_{K^+\pi^0\to K^+\eta}(s,t,u) \tag{22}$$

and similarly when the η' is in the final state. In terms of them one also has the scattering amplitudes for the t-crossed processes $K\bar{K} \to \pi\eta$ and $\pi\eta'$, which is pure $I = 1$. It reads

$$T^1(s,t,u) = -\sqrt{2}T_{K^+\pi^0\to K^+\eta}(t,s,u)\ , \tag{23}$$

and analogously for $K\bar{K} \to \pi\eta'$.

There are two isospin amplitudes in $K\bar{K} \to K\bar{K}$, that can be expressed as

$$\begin{aligned} T^0(s,t,u) &= 2D(s,t,u) + D(t,s,u)\,, \\ T^1(s,t,u) &= D(t,s,u)\,, \end{aligned} \tag{24}$$

with $D(s,t,u) = T_{K^+K^-\to K^0\bar{K}^0}(s,t,u)$. Notice that here we have derived both isospin amplitudes in terms of only one, while previous works used both $T_{K^+K^-\to K^0\bar{K}^0}(s,t,u)$ and $T_{K^+K^-\to K^+\bar{K}^-}(s,t,u)$ [49, 50, 51].

For $K\bar{K} \to \eta\eta$ and $K\eta \to K\eta$, the amplitudes involved read

$$\begin{aligned} T^0(s,t,u) &= -\sqrt{2}E(s,t,u)\ , \\ T^{\frac{1}{2}}(s,t,u) &= E(t,s,u)\,. \end{aligned} \tag{25}$$

with $E(s,t,u) = T_{K^0\bar{K}^0\to\eta\eta}(s,t,u)$. For $K\bar{K} \to \eta\eta', \eta'\eta'$ and $K\eta(\eta') \to K\eta$ and $K\eta'$, the formulas are analogous and the only difference is that one needs to redefine $E(s,t,u)$ for the corresponding process.

All the processes $\eta^{(\prime)}\eta^{(\prime)} \to \eta^{(\prime)}\eta^{(\prime)}$, with $\eta(')$ either an η or an η', are $I = 0$ and no crossing relation can be invoked to reduce the number of amplitudes needed, one for each process.

Next we can perform the partial wave projection for the isospin amplitudes and the convention we use is

$$T^I_J(s) = \frac{1}{2(\sqrt{2})^N}\int_{-1}^{1} dx\, P_J(x)\, T^I\big(s,t(x),u(x)\big)\,, \tag{26}$$

where $x = \cos\varphi$, with φ the scattering angle between the incoming and outgoing particles in the CM, and $P_J(x)$ stands for the Legendre polynomial. In the previous equation $(\sqrt{2})^N$ is a symmetry factor to account for identical particle states, such as $\pi\pi$ (with isospin 0, 1 or 2), $\eta\eta$ and $\eta'\eta'$. It corresponds to the so-called unitary normalization of Ref. [9]. E.g. $N = 1$ for $\pi\pi \to K\bar{K}$ and $N = 2$ for $\pi\pi \to \eta\eta$, and so on.

The unitarization method we follow was developed in Ref. [10] and is based on the N/D method [11]. The essential of this approach is to separate the crossed-channel cuts (LHC) and the right-hand cut (RHC), due to unitarity, in two different functions, $N(s)$ and $g(s)$. The former does not contain the two-particle unitarity cut but it has the LHC, while the later contains only the two-particle unitarity cut and not the LHC. A more detailed account of this unitarization method can be found in Refs. [10, 52, 53, 54]. Let us consider first the elastic case, its generalization to the coupled channel case is straightforward and given below. Because of unitarity above the two-particle threshold s_{th} a two-meson partial wave amplitude $T^I_J(s)$, with well-defined isospin I and angular momentum J, fulfills

$$\mathrm{Im}T^I_J(s) = T^I_J(s)\,\rho(s)\,T^I_J(s)^* \Rightarrow \mathrm{Im}T^I_J(s)^{-1} = -\rho(s)\,. \tag{27}$$

In the previous equation

$$\rho(s) = \frac{\sqrt{[s-(m_a+m_b)^2][s-(m_a-m_b)^2]}}{16\pi s}\,, \tag{28}$$

with m_a and m_b the masses of the two particles in the state. Eq. (27) implies that the imaginary part of the inverse of a partial wave is known. This can be used to write down a dispersion relation of the inverse of $T^I_J(s)$ taking as integration contour a circle of infinity radius that engulfs the right hand cut [10]. It then results

$$T^I_J(s)^{-1} = N^I_J(s)^{-1} + g(s) \ , \tag{29}$$

so that the function of $N^I_J(s)$, by construction, does not contain the RHC and $g(s)$ results from the known discontinuity along this cut, Eq. (27). In this way $g(s)$ is given by the following dispersion relation,

$$g(s) = g(s_0) - \frac{s-s_0}{\pi}\int_{s_{\rm th}}^{\infty} \frac{\rho(s')}{(s'-s)(s'-s_0)} ds' \, . \tag{30}$$

with

$$\mathrm{Im}\, g(s) = -\rho(s) \ , \tag{31}$$

for $s > s_{\rm th} = (m_a + m_b)^2$. The dispersive integral in Eq. (30) can be represented by the typical two-point one loop function [10]

$$\begin{aligned} x_\pm &= \frac{s+m_a^2-m_b^2}{2s} \pm \frac{1}{-2s}\sqrt{-4s(m_a^2 - i0^+) + (s+m_a^2-m_b^2)^2} \ , \\ 16\pi^2 g(s) &= a_{SL}(\mu) + \log\frac{m_b^2}{\mu^2} - x_+ \log\frac{x_+-1}{x_+} - x_- \log\frac{x_--1}{x_-} \, . \end{aligned} \tag{32}$$

For the case of equal mass scattering, $g(s)$ reduces to the simple form

$$16\pi^2\, g(s) = a_{SL}(\mu) + \log\frac{m^2}{\mu^2} - \sigma(s)\log\frac{\sigma(s)-1}{\sigma(s)+1} \, , \tag{33}$$

with

$$\sigma(s) = \sqrt{1-\frac{4m^2}{s}} \, . \tag{34}$$

In order to determine the interacting kernel $N^I_J(s)$ we proceed as explained in Refs. [52, 53], so that we match the unitarized amplitude Eq.(29) to the perturbative calculation, which is performed up to the one-loop level.[2] In this way, Eq. (29) should be expanded up to one power of $g(s)$. It then results for $N^I_J(s)$,

$$N^I_J(s) = T^I_J(s)^{(2)+\mathrm{Res}+\mathrm{Loop}} + T^I_J(s)^{(2)}\ g(s)\ T^I_J(s)^{(2)} \, . \tag{35}$$

Here $T^I_J(s)^{(2)+\mathrm{Res}+\mathrm{Loop}}$ stands for the partial wave amplitude from the perturbative calculation, with the superscripts (2), Res and Loop denoting the tree level amplitude from Eq. (1), resonance exchanges and loop contributions, respectively, depicted in Fig. 2. The wave-function renormalization and $\eta-\eta'$ mixing contributions are included in Res and Loop.

[2] Eq. (27) is valid below the first threshold of multi-particle states. Note that such states are further suppressed in the δ counting beyond our present one-loop calculation for the interaction kernel (they at least imply a two-loop calculation) and we do not consider them any longer.

It can be easily checked that $N_J^I(s)$ from Eq. (35) does not contain the RHC. This is due to the fact that the perburtative partial wave amplitudes satisfy perturbative unitarity

$$\begin{aligned} \mathrm{Im}\, T_J^I(s)^{(2)+\mathrm{Res}+\mathrm{Loop}} &= T_J^I(s)^{(2)}\ \rho(s)\ T_J^I(s)^{(2)} \\ &= -T_J^I(s)^{(2)}\ \mathrm{Im}\, g(s)\ T_J^I(s)^{(2)}\,, \end{aligned} \tag{36}$$

for $s > s_{\rm th}$. Regarding the LHC contribution, we would like to emphasize that it is perturbatively treated and collected in the $N_J^I(s)$ function defined in Eq.(35), unlike the RHC that we take into account non-perturbatively.

The previous formalism can be easily generalized to scattering processes with multiple coupled channels by employing a matrix notation. In this way, $T_J^I(s)$, $N_J^I(s)$ and $g(s) \to g_J^I(s)$ are now matrices and Eq. (29) still holds. Since phase space is diagonal then the matrix $g_J^I(s)$ is also diagonal, with its matrix elements given by Eq. (32), evaluated with the appropriate masses for the corresponding channel. The matrix $T_J^I(s)$ is symmetric, as required by time reversal invariance [3], which then implies from Eq. (29) that $N_J^I(s)$ is also symmetric.

Explicitly, for the $IJ = 00$ case there are five channels and the corresponding matrices read

$$N_0^0(s) = \begin{pmatrix} N_{\pi\pi\to\pi\pi} & N_{\pi\pi\to K\bar{K}} & N_{\pi\pi\to\eta\eta} & N_{\pi\pi\to\eta\eta'} & N_{\pi\pi\to\eta'\eta'} \\ N_{\pi\pi\to K\bar{K}} & N_{K\bar{K}\to K\bar{K}} & N_{K\bar{K}\to\eta\eta} & N_{K\bar{K}\to\eta\eta'} & N_{K\bar{K}\to\eta'\eta'} \\ N_{\pi\pi\to\eta\eta} & N_{K\bar{K}\to\eta\eta} & N_{\eta\eta\to\eta\eta} & N_{\eta\eta\to\eta\eta'} & N_{\eta\eta\to\eta'\eta'} \\ N_{\pi\pi\to\eta\eta'} & N_{K\bar{K}\to\eta\eta'} & N_{\eta\eta\to\eta\eta'} & N_{\eta\eta'\to\eta\eta'} & N_{\eta\eta'\to\eta'\eta'} \\ N_{\pi\pi\to\eta'\eta'} & N_{K\bar{K}\to\eta'\eta'} & N_{\eta\eta\to\eta'\eta'} & N_{\eta\eta'\to\eta'\eta'} & N_{\eta'\eta'\to\eta'\eta'} \end{pmatrix}, \tag{37}$$

$$g_0^0(s) = \begin{pmatrix} g_{\pi\pi} & 0 & 0 & 0 & 0 \\ 0 & g_{K\bar{K}} & 0 & 0 & 0 \\ 0 & 0 & g_{\eta\eta} & 0 & 0 \\ 0 & 0 & 0 & g_{\eta\eta'} & 0 \\ 0 & 0 & 0 & 0 & g_{\eta'\eta'} \end{pmatrix}. \tag{38}$$

For the $IJ = 1\,0$ channel, the matrices are

$$N_0^1(s) = \begin{pmatrix} N_{\pi\eta\to\pi\eta} & N_{\pi\eta\to K\bar{K}} & N_{\pi\eta\to\pi\eta'} \\ N_{\pi\eta\to K\bar{K}} & N_{K\bar{K}\to K\bar{K}} & N_{K\bar{K}\to\pi\eta'} \\ N_{\pi\eta\to\pi\eta'} & N_{K\bar{K}\to\pi\eta'} & N_{\pi\eta'\to\pi\eta'} \end{pmatrix}, \tag{39}$$

$$g_0^1(s) = \begin{pmatrix} g_{\pi\eta} & 0 & 0 \\ 0 & g_{K\bar{K}} & 0 \\ 0 & 0 & g_{\pi\eta'} \end{pmatrix}. \tag{40}$$

For the $IJ = \frac{1}{2}\ 0$ channel, it results

$$N_0^{\frac{1}{2}}(s) = \begin{pmatrix} N_{K\pi\to K\pi} & N_{K\pi\to K\eta} & N_{K\pi\to K\eta'} \\ N_{K\pi\to K\eta} & N_{K\eta\to K\eta} & N_{K\eta\to K\eta'} \\ N_{K\pi\to K\eta'} & N_{K\eta\to K\eta'} & N_{K\eta'\to K\eta'} \end{pmatrix}, \tag{41}$$

$$g_0^{\frac{1}{2}}(s) = \begin{pmatrix} g_{K\pi} & 0 & 0 \\ 0 & g_{K\eta} & 0 \\ 0 & 0 & g_{K\eta'} \end{pmatrix}. \tag{42}$$

Similar results hold for the $IJ = \frac{1}{2}\ 1$ channel.

For the $IJ = 1\,1$ quantum numbers we have

$$N_1^1(s) \ = \ \left(\begin{array}{cc} N_{\pi\pi\to\pi\pi} & N_{\pi\pi\to K\bar{K}} \\ N_{\pi\pi\to K\bar{K}} & N_{K\bar{K}\to K\bar{K}} \end{array} \right) , \tag{43}$$

$$g_1^1(s) \ = \ \left(\begin{array}{cc} g_{\pi\pi} & 0 \\ 0 & g_{K\bar{K}} \end{array} \right) . \tag{44}$$

Let us consider now the purely elastic channels where $N_J^I(s)$ and $g_J^I(s)$ are just functions, not matrices. For $IJ = \frac{3}{2}\ 0$, one has

$$N_0^{\frac{3}{2}}(s) \ = N_{K\pi\to K\pi} \, , \tag{45}$$

$$g_0^{\frac{3}{2}}(s) \ = g_{K\pi} \, . \tag{46}$$

For $IJ = 2\ 0$,

$$N_0^2(s) \ = N_{\pi\pi\to\pi\pi} \, ,$$

$$g_0^2(s) \ = g_{\pi\pi} \, . \tag{47}$$

Finally, the appropriate functions for $IJ = 0\ 1$ are

$$N_1^0(s) \ = N_{K\bar{K}\to K\bar{K}} \, ,$$

$$g_1^0(s) \ = g_{K\bar{K}} \, . \tag{48}$$

After having the unitarized scattering amplitude from Eq. (29), the S-matrix for the IJ channel, $S_J^I(s)$, can be defined straightforwardly in matrix notation

$$S_J^I = 1 + 2i\sqrt{\rho_J^I(s)} \cdot T_J^I(s) \cdot \sqrt{\rho_J^I(s)} \, . \tag{49}$$

with $\rho_J^I(s) = -\mathrm{Im} g_J^I(s)$. From the matrix elements of the S-matrix we can read out the phase shifts δ_{kk} and δ_{kl}, with $k \neq l$, since

$$\begin{aligned} S_{kk} &= |S_{kk}| e^{2i\delta_{kk}} \, , \\ S_{kl} &= |S_{kl}| e^{i\delta_{kl}} \, . \end{aligned} \tag{50}$$

5 Discussion and results

In this section we first discuss the fit to experimental data in order to fix the free parameters in our approach. Later we discuss the associated spectroscopy and its properties under variation of N_C.

5.1 Fit Quality

We perform the fit for the $IJ = 00$ channel up to $\sqrt{s} = 1300$ MeV. The inclusion of the η' meson is not enough to guarantee that our current calculation can be applied higher in the energy region. There are good phenomenological reasons to expect that the 4π state plays an important at this energy level and its influence can not be simply neglected [12]. The observables fitted are shown in Fig. 5 and correspond to the elastic $\pi\pi \to \pi\pi$ phase shifts, $\delta^{00}_{\pi\pi\to\pi\pi}$, the elasticity parameter, $|S^{00}_{\pi\pi\to\pi\pi}|$, and the phase and one half of the modulus of the S-matrix element for the inelastic process $\pi\pi \to K\bar{K}$ above the $K\bar{K}$ threshold, $\delta^{00}_{\pi\pi\to K\bar{K}}$ and $\frac{1}{2}|S^{00}_{\pi\pi\to K\bar{K}}|$, respectively. For references to the experimental data see Fig. 5.

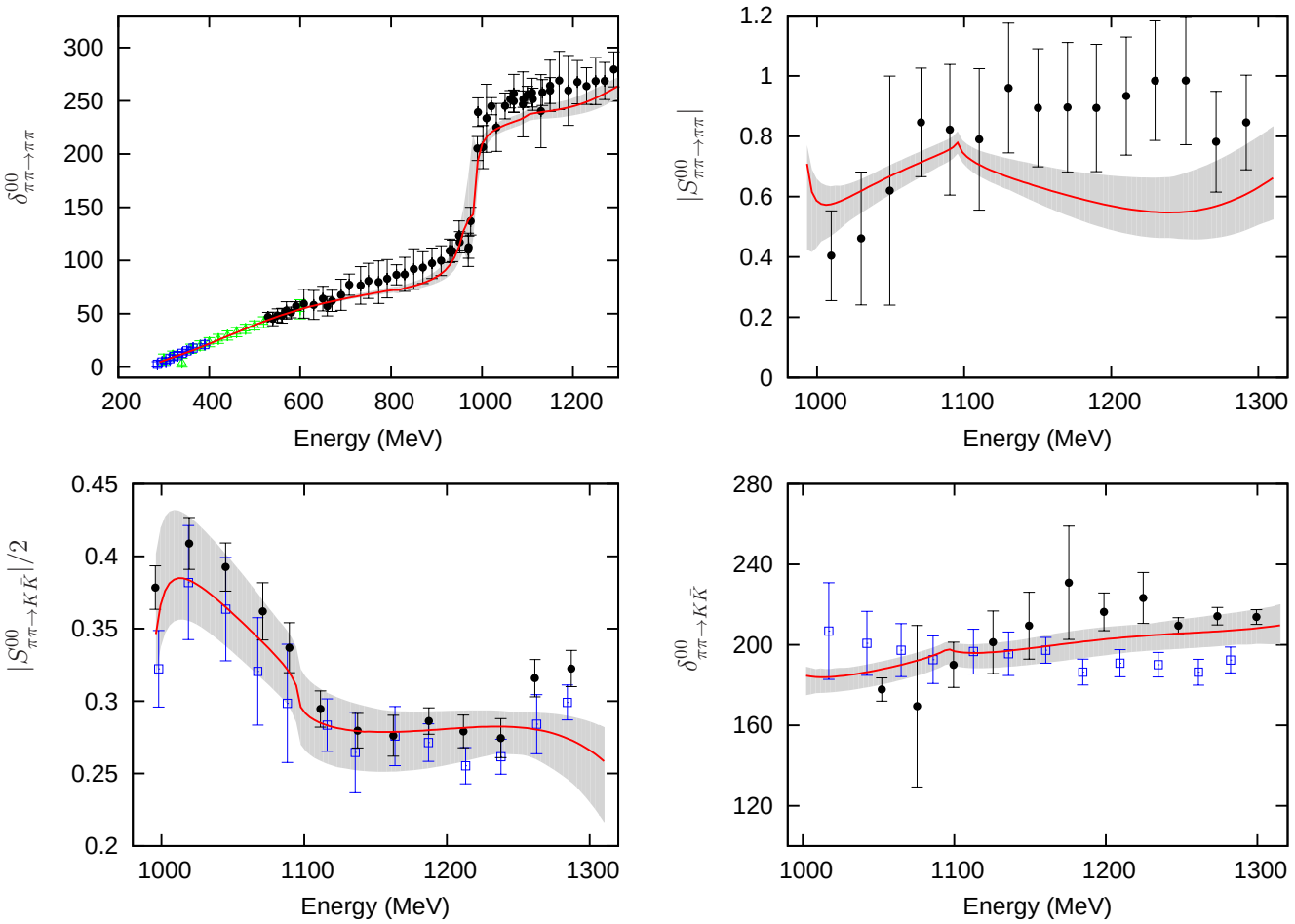

Figure 5: (Color online.) Plots of the fit to the $IJ = 00$ case. From top to bottom and left to right: the phase shifts of $\pi\pi \to \pi\pi$ ($\delta^{00}_{\pi\pi\to\pi\pi}$), the modulus of the S-matrix element for $\pi\pi \to \pi\pi$ ($|S^{00}_{\pi\pi\to\pi\pi}|$), the half modulus of the S-matrix element for $\pi\pi \to K\bar{K}$ ($|S^{00}_{\pi\pi\to K\bar{K}}|/2$) and the phase shifts of $\pi\pi \to K\bar{K}$ ($\delta^{00}_{\pi\pi\to K\bar{K}}$). $\delta^{00}_{\pi\pi\to\pi\pi}$ data correspond to Ref. [55] (triangle in green), [56] (square in blue) and the average data from Refs. [57, 58, 59](circle in black), as employed in Ref. [10]. $|S^{00}_{\pi\pi\to\pi\pi}|$ is from Ref. [57]. $|S^{00}_{\pi\pi\to K\bar{K}}|/2$ is from Refs. [60](square in blue) and [61](circle in black). The phase shifts $\delta^{00}_{\pi\pi\to K\bar{K}}$ are from Refs. [60](square in blue), [62](circle in black). The solid (red) line corresponds to the best fit, while the error bands are presented by the shadowed area. This notation also applies in Figs. 6 and 7.

For the $IJ = \frac{1}{2}\,0$ channel, since there is no significant inelasticity above the $K\eta'$ threshold, we fit the data up to $\sqrt{s} = 1600$ MeV. Although for higher energies one already has the influence of the $K_0^*(1950)$ resonance [41] which we have not included. The observables in the fit are the $K\pi \to K\pi$ phase shifts $\delta^{\frac{1}{2}0}_{K\pi\to K\pi}$. The reference to experimental data is given in Fig. 6.

For the $IJ = 1\,0$ channel, there are no available data for scattering up to now and it is typical to use a $\pi\eta$ event distribution from other production processes to obtain information on the $a_0(980)$ resonance. As the production mechanism is not under good theoretical control in our work, we decide to fit the data around the resonance region up to 1050 MeV, as explained below. The experiment data for the $\pi\eta$ distribution are illustrated in Fig. 6.

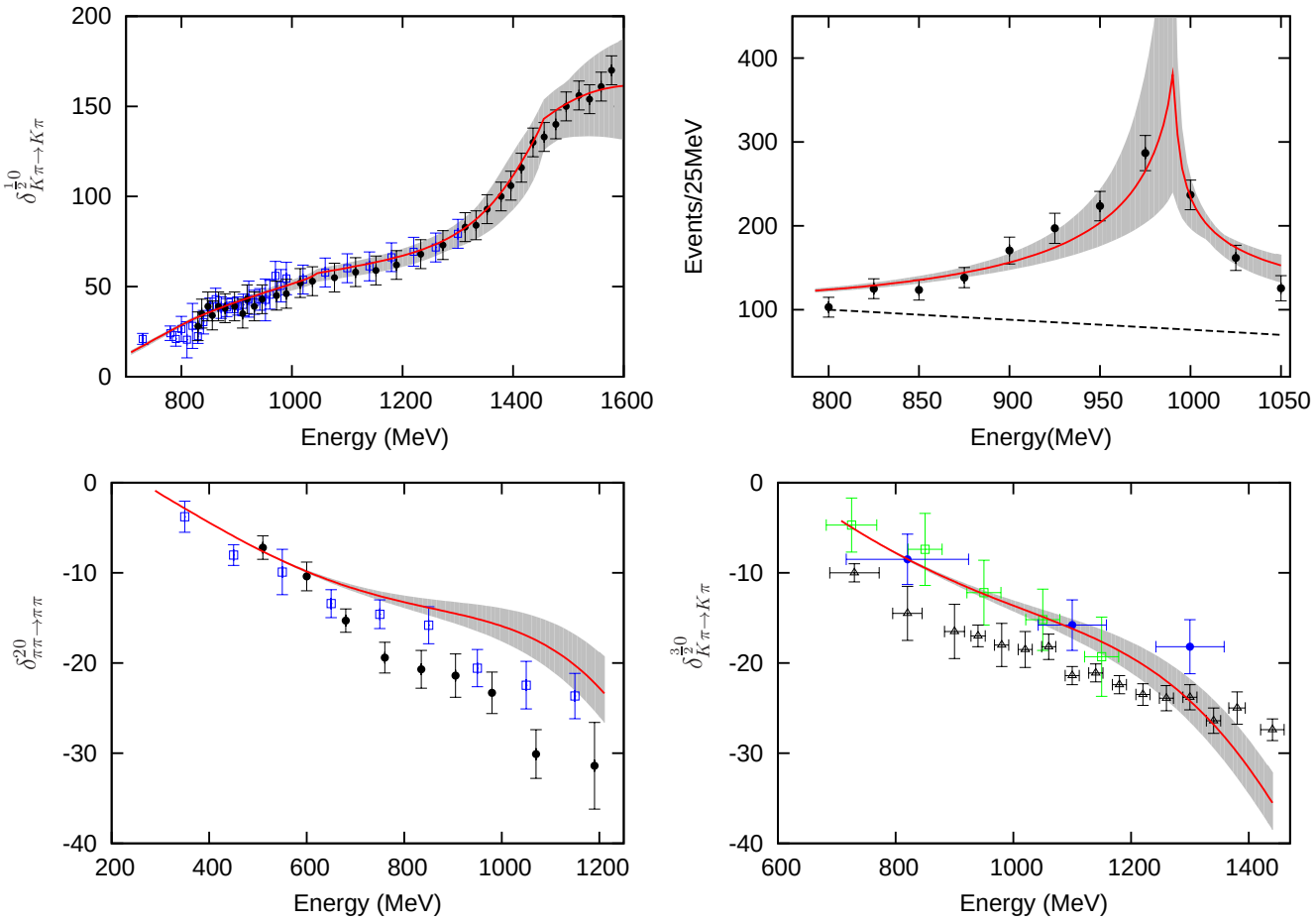

Figure 6: (Color online.) From top to bottom and left to right: phase shifts of $K\pi \to K\pi$ with $IJ = \frac{1}{2}\,0$ ($\delta^{\frac{1}{2}0}_{K\pi\to K\pi}$), $\pi\eta$ event distribution with $IJ = 1\,0$, phase shifts of $\pi\pi \to \pi\pi$ with $IJ = 2\,0$ ($\delta^{20}_{\pi\pi\to\pi\pi}$) and phase shifts of $K\pi \to K\pi$ with $IJ = \frac{3}{2}\,0$ ($\delta^{\frac{3}{2}0}_{K\pi\to K\pi}$). $\delta^{\frac{1}{2}0}_{K\pi\to K\pi}$ corresponds to the average data from Refs. [63, 64, 65] (square in blue), as used in Ref. [10], and Ref.[66](circle in black). Data for the $\pi\eta$ event distribution are from Ref. [67] and the dashed line corresponds to the background [10]. $\delta^{20}_{\pi\pi\to\pi\pi}$ is from Refs. [68](square in blue) and [69](circle in black). The experimental data for $\delta^{\frac{3}{2}0}_{K\pi\to K\pi}$ are taken from Refs. [70](square in green), [71](circle in blue) and [64](triangle in black).

For the exotic channels with $IJ = \frac{3}{2}\,0$ and $IJ = 2\,0$, we fit the phase shifts of $K\pi \to K\pi$ and $\pi\pi \to \pi\pi$, respectively. The references for the experimental data are given in Fig. 6.

The observables we fit in $IJ = 1\,1$ and $IJ = \frac{1}{2}\,1$ are the phase shifts of $\pi\pi \to \pi\pi$ and $K\pi \to K\pi$, $\delta^{11}_{\pi\pi\to\pi\pi}$ and $\delta^{\frac{1}{2}1}_{K\pi\to K\pi}$, in order. They are fitted up to 1200 MeV, as we only include the lowest multiplet of vector resonances in the Lagrangian Eq.(6). The references to experimental data can be found in Fig. 7.

Before moving to the details of the phenomenological discussion, let us first comment on the free parameters in our theory. Apart from the couplings in Eqs.(5), (6) and (11), there are the bare mass parameters of the resonances, the $U_A(1)$ anomaly mass M_0 in Eq.(1) and the subtraction constants a_{SL} defined in Eq.(32) for different channels. One way to reduce the number of the subtraction constants is to impose the isospin symmetry for them [72]. In this way, a_{SL} of $g_{\pi\pi}$ in $IJ = 0\,0$ and in $IJ = 2\,0$ are the same. Similarly, $g_{K\bar{K}}$ in $IJ = 0\,0$ and $IJ = 1\,0$ are also equal. This also applies to $g_{K\pi}$ in $IJ = \frac{1}{2}\,0$ and in $IJ = \frac{3}{2}\,0$. In principle, the subtraction constants in the remaining channels are free. Nevertheless, if one further assumes $U(3)$ symmetry within each partial wave the values of different subtraction constants should be also equal. We indeed exploit this feature as much as we can in the numerical discussion. We summarize the subtraction constants used in the fits discussed below:

$$\begin{aligned}
&a^{00}_{SL} = a^{00,\pi\pi}_{SL} = a^{00,K\bar{K}}_{SL} = a^{00,\eta\eta}_{SL} = a^{00,\eta\eta'}_{SL} = a^{00,\eta'\eta'}_{SL} = a^{20,\pi\pi}_{SL}\,,\\
&a^{\frac{1}{2}0}_{SL} = a^{\frac{1}{2}0,K\pi}_{SL} = a^{\frac{1}{2}0,K\eta}_{SL} = a^{\frac{1}{2}0,K\eta'}_{SL} = a^{\frac{3}{2}0,K\pi}_{SL}\\
&a^{10,\pi\eta'}_{SL} = a^{10,K\bar{K}}_{SL} = a^{00,K\bar{K}}_{SL}\,,\\
&a^{10,\pi\eta}_{SL}\,,
\end{aligned} \tag{51}$$

and all of the subtraction constants in the vector channels are set equal to a^{00}_{SL}.

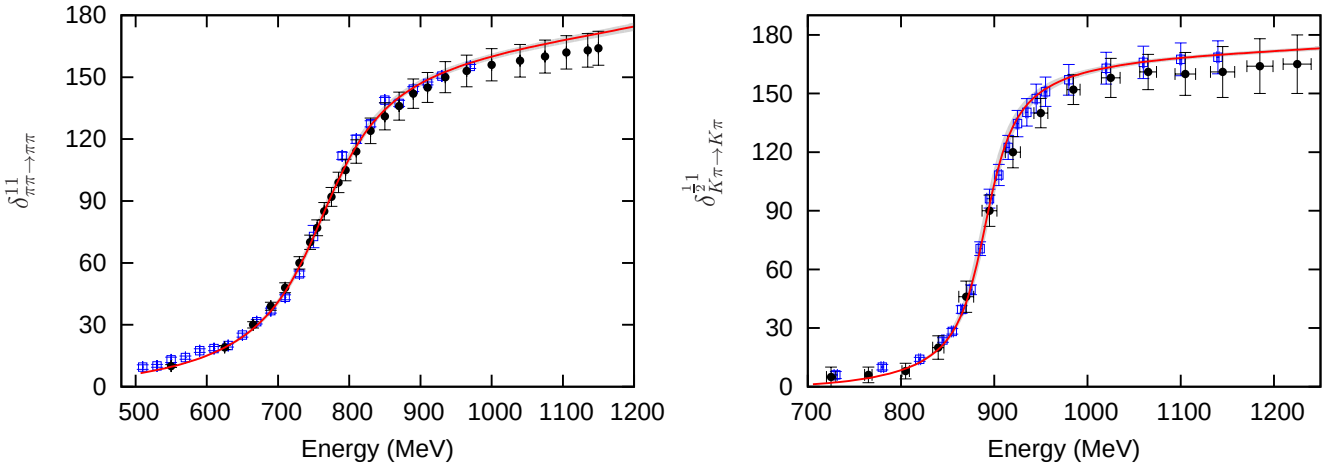

Figure 7: (Color online.) Plots from the fit to the vector channels. The left panel is for the $IJ = 11$ channel and the right one is for $IJ = \frac{1}{2}1$. The data of phase shifts for $\pi\pi \to \pi\pi$ with $IJ = 11$, $\delta^{11}_{\pi\pi\to\pi\pi}$ are from Refs. [73](square in blue) and [74](circle in black). The data of phase shifts for $K\pi \to K\pi$ with $IJ = \frac{1}{2}1$, $\delta^{\frac{1}{2}1}_{K\pi\to K\pi}$ are from Refs. [63](circle in black) and [64](square in blue).

In order to fit the $\pi\eta$ mass distribution we need to introduce two additional parameters to parameterize

the production mechanism, $\mathcal{N}$ and c, that enter in the expression

$$\frac{dN_{\pi\eta}}{dE_{\pi\eta}} = q_{\pi\eta}\,\mathcal{N}\big|\,T_{K\bar{K}\to\pi\eta}(s) + c\,T_{\pi\eta\to\pi\eta}(s)\,\big|^2\,. \tag{52}$$

Here, $q_{\pi\eta}$ is the three momentum of $\pi\eta$ system in CM and $E_{\pi\eta} = \sqrt{s}$ is the energy in the same frame. The parameter $\mathcal{N}$ accounts for the fact that the event distribution is not normalized. The linear combination of amplitudes in the previous equation originates because the $a_0(980)$ shows up differently in them. See also Ref. [52] for a more detailed explanation of the derivation of Eq. (52) in connection with the invariant mass distribution of $\bar{K}N$ around the $\Lambda(1405)$ resonance.

In the end, we have 16 free parameters and the fitted results are

$$\begin{aligned}
&c_d = (15.6^{+4.2}_{-3.4})\,\text{MeV}\,, && c_m = (31.5^{+19.5}_{-22.5})\,\text{MeV}\,,\\
&\widetilde{c}_d = (8.7^{+2.5}_{-1.7})\,\text{MeV}\,, && \widetilde{c}_m = (15.8^{+3.3}_{-3.0})\,\text{MeV}\,,\\
&M_{S_8} = (1370^{+132}_{-57})\,\text{MeV}\,, && M_{S_1} = (1063^{+53}_{-31})\,\text{MeV}\,,\\
&M_\rho = (801.0^{+7.0}_{-7.5})\,\text{MeV}\,, && M_{K^*} = (909.0^{+7.5}_{-6.9})\,\text{MeV}\,,\\
&G_V = (61.9^{+1.9}_{-1.9})\,\text{MeV}\,, && a_{SL}^{1\,0,\pi\eta} = 2.0^{+3.1}_{-3.4}\,,\\
&a_{SL}^{00} = (-1.15^{+0.07}_{-0.09})\,, && a_{SL}^{\frac{1}{2}\,0} = (-0.96^{+0.10}_{-0.16})\,,\\
&\mathcal{N} = (0.6^{+0.3}_{-0.3})\,\text{MeV}^{-2}\,, && c = (1.0^{+0.6}_{-0.4})\,,\\
&M_0 = (954^{+102}_{-95})\,\text{MeV}\,, && \Lambda_2 = (-0.6^{+0.5}_{-0.4})\,,
\end{aligned} \tag{53}$$

with $\chi^2/\text{d.o.f} = 714/(348-16) \simeq 2.15$.

The corresponding figures from the fit are displayed in Figs. 5, 6 and 7. The width of the bands shown and the errors given in the fitted parameters in Eq. (53) represent our statistical uncertainties at the level of two standard deviations [62]

$$n_\sigma = \Delta\chi^2/(2\chi_0^2)^{1/2}\,, \tag{54}$$

being χ_0^2 the minimum of the χ^2 obtained corresponding to the best fit, n_σ the number of standard deviations and $\Delta\chi^2 = \chi^2 - \chi_0^2$.

As one can see in Figs. 5, 6 and 7, most of the observables are well reproduced through the fit. The phase shifts of $\pi\pi \to \pi\pi$ with $IJ = 00$ in the low energy region from the recent measurement of K_{e4} decay [56] are included in our fit and they can be perfectly reproduced. For the $\pi\eta$ invariant mass distribution, we explicitly subtract the background as analyzed in Ref. [67], which are mainly caused by the tail of higher resonances. Compared with observables in the scalar channels, the errors in the vector channels are rather small. Among all of the curves, the least satisfactory results from our fit correspond to the channels with exotic quantum numbers with $IJ = 20$ and $IJ = \frac{3}{2}0$, which is also an important source for the χ^2 resulting from our fit. For example, with 42 data points, they contribute 281 to the total χ^2, i.e. 12% of degrees of freedom carry 39% of the χ^2. Nevertheless, one also has to remark that the different experimental data in these channels are not always compatible at the level of one σ, which also makes the χ^2 to increase. On the other hand, since no resonances appear in those exotic channels, it may indicate that unitarity is less important as compared with the other channels. In contrast, the LHC contribution could play a more important role in this case [10, 41]. We recall that precisely our unitarization scheme only incorporates the LHC effects perturbatively. Thus, an improvement on the treatment of the LHC should provide a better fit for these two channels.

With the fitted parameters in Eq. (53) we can also calculate the values for the masses of the η and η' that are obtained by diagonalizing Eq. (13). We then obtain from Eq. (17) the values

$$m_\eta = (526^{+33}_{-41})\,\text{MeV}\,, \qquad m_{\eta'} = (951^{+47}_{-60})\,\text{MeV}\,. \tag{55}$$

The leading order mixing angle of $\eta - \eta'$ that results from Eq. (1) is

$$\theta = -16.2^{\circ}{}^{+2.8^{\circ}}_{-2.9^{\circ}} \, . \tag{56}$$

Concerning the resonance parameter c_d in Eq.(53), the value from our fit is a bit smaller than the previous determinations, such as $c_d = 19.1^{+2.4}_{-2.1}$ MeV given in Ref. [10], $c_d = 23.8$ MeV reported in Ref. [41] and $c_d = (26 \pm 7)$ MeV in Ref. [75]. Nevertheless, they are compatible within the error bands. For the coupling c_m, though different approaches predict a broad range for its central value, they always accompany a large error, for example $c_m = 31.5^{+19.5}_{-22.5}$ MeV in the present case, $c_m = (15 \pm 30)$ MeV in Ref. [10] and $c_m = (80 \pm 20)$ MeV given in Ref. [75]. Comparing the couplings related to the singlet scalar with Ref. [10], our determination of $\widetilde{c}_m$ is compatible with $\widetilde{c}_m = 10.6^{+4.5}_{-3.5}$ MeV in Ref. [10], while for $\widetilde{c}_d$ the current fit leads to a smaller value, compared with $\widetilde{c}_d = 20.9^{+1.6}_{-1.0}$ MeV given in the same reference. For the bare masses of resonances, our present results agree well with the previous determinations: $M_{S_8} = (1390 \pm 20)$ MeV, $M_{S_1} = (1020^{+40}_{-20})$ MeV in Ref. [10] and $M_{S_8} = 1400$ MeV in Ref. [41]. Our values in Eq. (53) are compatible with the estimates $\widetilde{c}_d \simeq c_d/\sqrt{3}$ and $\widetilde{c}_m \simeq c_m/\sqrt{3}$ based on large N_C [44], however the bare masses for the singlet and octet scalar resonances are clearly different, as obtained in previous studies [10, 12]. The current determination for the subtraction constant a_{SL} is consistent with the previous result in Ref.[10] as well. For the vector resonance coupling G_V, our result is in good agreement with $G_V = (63.9 \pm 0.6)$ MeV determined in Ref. [75]. The $U_A(1)$ anomaly mass M_0 carries a large error and agrees with the conclusion in Ref. [76]. The $1/N_C$ suppressed parameter Λ_2 is poorly known in literature and in Ref. [43] $\Lambda_2 = 0.3$ is estimated, which is somewhat incompatible with ours. Nevertheless in Ref. [43] the value of Λ_2 is not determined by any physical observables, but only by naive dimensional analysis. Moreover in their case the counterterm Λ_2 is always accompanied by the factor of m_π^2, indicating the insensitivity of this parameter there.

5.2 Resonances generated from unitarized amplitudes

We summarize the masses, widths and residues of the various resonances in Table 1. Resonances are characterized by their pole positions in the partial wave amplitudes in unphysical Riemann sheets. Around a resonance pole s_R, corresponding to a resonance R, the partial wave amplitude $T^I_J(s)_{i\to j}$ tends to

$$T^I_J(s)_{i\to j} \to -\frac{g_{R\to i}\, g_{R\to j}}{s - s_R^2} \, . \tag{57}$$

By calculating the residue of the resonance pole we then obtain the product of the couplings to the corresponding decay modes. At the practical level we calculate the residues by applying the Cauchy integral formula

$$g_{R\to i}\, g_{R\to j} = -\frac{1}{2\pi i} \oint_{|s-s_R|\to 0} T^I_J(s)_{i\to j}\, ds \, . \tag{58}$$

For every pole one has further to indicate in which unphysical Riemann sheet it lies. Each function $g(s)$ has 2 sheets and their relation is given by [9]

$$g_{II}(s) = g_I(s) + 2i\rho(s) \, , \tag{59}$$

with $g_{II}(s)$ the function analytically extrapolated to its second Riemann sheet and $g_I(s)$ the function in its first Riemann sheet, given in Eq. (32). Different Riemann sheets are easily accessed by deciding on which sheet every $g_i(s)$ function, associated to channel i, is calculated. In this way, for an IJ channel there are 2^N possible sheets, with N the number of coupled states with the same IJ quantum numbers.

R	M (MeV)	$\Gamma/2$ (MeV)	$\lvert\text{Residues}\rvert^{1/2}$ (GeV)	Ratios	
σ	440^{+3}_{-3}	258^{+2}_{-3}	$3.02^{+0.03}_{-0.03}$ $(\pi\pi)$	$0.51^{+0.03}_{-0.02}$ $(KK/\pi\pi)$	$0.06^{+0.03}_{-0.01}$ $(\eta\eta/\pi\pi)$
				$0.16^{+0.03}_{-0.02}(\eta\eta'/\pi\pi)$	$0.05^{+0.05}_{-0.03}(\eta'\eta'/\pi\pi)$
$f_0(980)$	981^{+9}_{-7}	22^{+5}_{-7}	$1.7^{+0.3}_{-0.3}(\pi\pi)$	$2.3^{+0.3}_{-0.2}(KK/\pi\pi)$	$1.6^{+0.3}_{-0.3}(\eta\eta/\pi\pi)$
				$1.2^{+0.1}_{-0.2}(\eta\eta'/\pi\pi)$	$0.7^{+0.4}_{-0.5}(\eta'\eta'/\pi\pi)$
$f_0(1370)$	1401^{+58}_{-37}	106^{+36}_{-23}	$2.4^{+0.2}_{-0.1}(\pi\pi)$	$0.62^{+0.04}_{-0.05}(KK/\pi\pi)$	$0.9^{+0.1}_{-0.1}(\eta\eta/\pi\pi)$
				$1.7^{+0.4}_{-0.6}(\eta\eta'/\pi\pi)$	$1.1^{+0.4}_{-0.6}(\eta'\eta'/\pi\pi)$
κ	665^{+9}_{-9}	268^{+21}_{-6}	$4.2^{+0.2}_{-0.2}(K\pi)$	$0.7^{+0.1}_{-0.1}(K\eta/K\pi)$	$0.5^{+0.1}_{-0.1}(K\eta'/K\pi)$
$K_0^*(1430)$	1428^{+56}_{-23}	87^{+53}_{-28}	$3.3^{+0.5}_{-0.4}(K\pi)$	$0.54^{+0.07}_{-0.02}$ $(K\eta/K\pi)$	$1.2^{+0.2}_{-0.3}(K\eta'/K\pi)$
$a_0(980)$	1012^{+25}_{-7}	16^{+50}_{-13}	$2.5^{+1.3}_{-0.8}(\pi\eta)$	$1.9^{+0.2}_{-0.3}$ $(KK/\pi\eta)$	$0.01^{+0.03}_{-0.01}(\pi\eta'/\pi\eta)$
$a_0(1450)$	1368^{+68}_{-68}	71^{+48}_{-23}	$2.3^{+0.4}_{-0.5}(\pi\eta)$	$0.6^{+0.7}_{-0.2}(KK/\pi\eta)$	$0.6^{+0.2}_{-0.1}(\pi\eta'/\pi\eta)$
$\rho(770)$	762^{+4}_{-4}	72^{+2}_{-2}	$2.48^{+0.03}_{-0.05}(\pi\pi)$	$0.64^{+0.01}_{-0.01}(KK/\pi\pi)$	
$K^*(892)$	891^{+3}_{-4}	25^{+2}_{-1}	$1.86^{+0.05}_{-0.05}(K\pi)$	$0.91^{+0.03}_{-0.02}(K\eta/K\pi)$	$0.45^{+0.08}_{-0.08}(K\eta'/K\pi)$
$\phi(1020)$	$1014.7^{+0.3}_{-0.3}$	$1.50^{+0.04}_{-0.08}$	$0.79^{+0.01}_{-0.02}(K\bar{K})$		

Table 1: Pole positions for the different resonances in $\sqrt{s} \equiv (\text{M}, -i\frac{\Gamma}{2})$. The mass (M) and the half width ($\Gamma/2$) are given in units of MeV. The modulus of the square root of a residue is given in units of GeV, which corresponds to the coupling of the resonance with the first channel (specified inside the parentheses). The last two columns are the ratios of the coupling strengths of the same resonance to the remaining channels with respect to the first one. The corresponding Riemann sheets where the resonance poles are located are explained in detail in the text. Note that here the residues for $\pi\pi$, $\eta\eta$ and $\eta'\eta'$ are given in the unitary normalization, due to the extra factors of $\sqrt{2}$ dividing Eq. (26). Thus, one should multiply by $\sqrt{2}$ these couplings if one wishes to restore standard physical normalization to 1 for these states. The error bands of the resonance parameters appearing in the table only correspond to the statistical error from the fit in Eq.(53).

Along the real s-axis above threshold changing sheet implies to reverse the sign of the imaginary part of the $g_i(s)$ function. In the following we conventionally label the physical or first Riemann sheet as $(+,+,+,\ldots)$. The second Riemann sheet can be reached by changing the sign of the first threshold, which is labeled as $(-,+,+,+,\ldots)$. The third, fourth and fifth sheets, also considered in this work, correspond to $(-,-,+,+,\ldots)$, $(+,-,+,+,\ldots)$ and $(-,-,-,+,\ldots)$. More sheets can be obtained by taking more combinations of plus and minus signs between the brackets. At a given energy value $\sqrt{s}$, there is one unphysical sheet to which one can directly access from the physical sheet by crossing from $s+i0^+$ to $s-i0^+$ the branch cut between the two thresholds T_n and T_{n+1}, with $T_n < \sqrt{s} < T_{n+1}$. In our current notations, this specific unphysical sheet corresponds to changing the signs of all the thresholds below the considered energy point $\sqrt{s}$, i.e

$$(\underbrace{-,-,..-}_{n},+,+,\ldots) \tag{60}$$

In fact this is also the most relevant Riemann sheet where one should search the pole for a given resonance affecting that energy region, although other shadow poles may also appear in other unphysical sheets [77]. Thus in the following, we mainly present our findings on the complex plane in this specific sheet for a

given resonance and simply comment the results appearing in other unphysical sheets.

Through the unitarization procedure described previously, we can simultaneously get the relevant resonances in the considered energy region, such as σ, $f_0(980)$ and $f_0(1370)$ in the $IJ = 00$ channel, κ and $K_0^*(1430)$ in $IJ = \frac{1}{2}\,0$, $a_0(980)$ and $a_0(1450)$ in $IJ = 1\,0$, $\phi(1020)$ in $IJ = 01$, $\rho(770)$ in $IJ = 11$ and $K^*(892)$ with $IJ = \frac{1}{2}\,1$. The pole positions and residues of these resonances are collected in Table 1. We comment on them channel by channel next.

$IJ = 00$

Three kinds of resonance poles in the complex plane have been found, which we identify with the σ, $f_0(980)$ and $f_0(1370)$ resonances. According to our previous discussion, the most relevant Riemann sheets for σ, $f_0(980)$ and $f_0(1370)$ correspond to the ones with $(-,+,+,+,+)$, $(-,+,+,+,+)$ and $(-,-,-,+,+)$, respectively. Their pole positions are compatible within errors with those given in the PDG [1]. For the $f_0(1370)$ resonance, shadow poles are observed in the sheets labeled with $(-,+,+,+,+)$ and $(-,-,+,+,+)$ as well, whose positions are found to be $\sqrt{s} = (1273^{+33}_{-29} - 103^{+46}_{-14}\,i)$ MeV and $\sqrt{s} = (1330^{+34}_{-29} - 136^{+42}_{-24}\,i)$ MeV, in order, compared with $\sqrt{s} = (1401^{+58}_{-37} - 106^{+36}_{-23}\,i)$ MeV in the sheet $(-,-,-,+,+)$.

From the residues given in Table 1, one can see that the biggest coupling of the σ resonance is to the $\pi\pi$ channel. Nonetheless, it also has a large coupling to the $K\bar{K}$ channel, so that the coupling to K^+K^- is large. This is also the case in Ref. [78], though there this is interpreted as an indication that the σ resonance has a strong glueball component. In general the $\eta\eta$, $\eta\eta'$ and $\eta'\eta'$ are weakly coupled to σ, but not to $f_0(980)$ and $f_0(1370)$. The $f_0(980)$ resonance has its strongest coupling to $K\bar{K}$, though it also couples almost as equally strong to $\eta\eta$. Notice that the ratios of the couplings to $K\bar{K}$ and $\pi\pi$ between the σ and $f_0(980)$ are nearly inverse each other. The importance of the $\eta\eta$ channel for understanding properly the $f_0(980)$ was stressed in Ref. [10], because once this channel is considered the inclusion of a bare single state around 1 GeV is required [10, 12, 79]. The $f_0(980)$ pole in fact moves continuously to the bare state around 1 GeV if the $g_0^0(s)$ matrix is removed, e.g. by multiplying it with a factor $\lambda \in [0,1]$. The $f_0(1370)$ resonance owns its origin to the octet scalar σ_8 with the bare mass of 1370 MeV, as already noticed in Ref. [12]. These bare poles gain their widths through the unitarization procedure. However, a proper study of the $f_0(1370)$ resonance requires to include explicitly the 4π channel [12]. For the σ pole there is no corresponding bare state at the Lagrangian level and it is mainly generated by the strong interactions between pseudo-Goldstone bosons. This is partially the case for the $f_0(980)$ because the strong $K\bar{K}$ interactions give rise to a bound state close to the actual mass of this resonance [9, 80, 81, 82, 83]. These conclusions are further supported by the N_C trajectories of those poles, which we will discuss later.

$IJ = \frac{1}{2}\,0$

For these quantum numbers we obtain two poles corresponding to the κ and $K_0^*(1430)$ resonances. The most relevant Riemann sheets correspond to $(-,+,+)$ and $(-,-,+)$ respectively. Their pole positions are compatible with those in the PDG [1]. In the fourth Riemann sheet, i.e with $(+,-,+)$, a shadow pole at $\sqrt{s} = (717^{+8}_{-5} - 280^{+30}_{-24}\,i)$ MeV is found for the κ resonance, compared with the second sheet pole located at $\sqrt{s} = (665^{+9}_{-9} - 268^{+21}_{-6}\,i)$ MeV. For the $K_0^*(1430)$ resonance, two shadow poles are found in the $(-,+,+)$ and $(-,-,-)$ sheets, with $\sqrt{s} = (1420^{+132}_{-49} - 154^{+95}_{-57}\,i)$ MeV and $\sqrt{s} = (1352^{+74}_{-29} - 114^{+60}_{-39}\,i)$ MeV, respectively, compared with $\sqrt{s} = (1428^{+56}_{-23} - 87^{+53}_{-28}\,i)$ MeV in the sheet $(-,-,+)$.

We also find a good agreement with the previous study of Ref. [41] that shares for this channel many facts in common with ours. The κ resonance, similar to the case of σ, is generated mainly from the

pseudo-Goldstone interactions. The $K_0^*(1430)$ pole originates from the bare octet of scalar resonances in the Lagrangian Eq. (5). Again, these conclusions are further supported below when discussing the N_C dependence of the pole positions.

$IJ = 1\,0$

This is the most problematic channel in our analysis. By imposing the $U(3)$ symmetry on the subtraction constants, i.e. with the constraint of $a_{SL}^{10,\pi\eta} = a_{SL}^{10,K\bar{K}} = a_{SL}^{10,\pi\eta'}$, no good fit for this channel could be obtained simultaneously with the other data. We have checked that the influence of the $\pi\eta'$ channel to the mass distribution of $\pi\eta$ Eq. (52) is actually tiny. Within a reasonable range for the $\pi\eta$ subtraction constant the best fit prefers positive values, in contrast with the negative ones for the other channels, though the error for this parameter is large. However, we notice that, similarly to previous studies [9, 10], if only the tree level amplitudes are taken for the interacting kernel one can fit well the same data and get a reasonable pole for the $a_0(980)$ resonance on the second sheet. Also a similar negative value for the $\pi\eta$ subtraction constant results then as in the other channels, with the constraint $a_{SL}^{10,\pi\eta} = a_{SL}^{10,K\bar{K}} = a_{SL}^{10,\pi\eta'}$ [10].

We show in Table 1 the $a_0(980)$ and $a_0(1450)$ pole positions and residues. For $a_0(980)$, the most relevant sheet should correspond to the one with $(-,+,+)$ or $(-,-,+)$. However with our current best fit, no reasonable poles are found in those Riemann sheets. Nevertheless, a pole located in the fourth sheet, i.e. with $(+,-,+)$, shows up and we identify it as the $a_0(980)$ resonance, whose pole position can be found in Table 1.

The most relevant Riemann sheet for the $a_0(1450)$ corresponds to the one with $(-,-,-)$, since its mass is larger than the $\pi\eta'$ threshold. Similarly as for the $f_0(1370)$ and $K_0^*(1430)$ resonances, we find two shadow poles for $a_0(1450)$ in the sheets with $(-,+,+)$ and $(-,-,+)$, located at $\sqrt{s} = (1354^{+48}_{-59} - 44^{+60}_{-34}\,i)$ MeV and $\sqrt{s} = (1369^{+63}_{-64} - 56^{+45}_{-21}\,i)$ MeV respectively, compared with $\sqrt{s} = (1368^{+68}_{-68} - 71^{+48}_{-23}\,i)$ MeV in the $(-,-,-)$ sheet. Other channels are lacking at the typical energies for the $a_0(1450)$, as listed in the PDG [1] for its decay widths. This lack of decay channels (e.g. $\omega\pi\pi$ and $a_0(980)\pi\pi$) explains why our pole position for this resonance gives a smaller width than in [1]. In addition, no two-body scattering data are available for this channel which also reduces its statistical weight in the fits performed.

$IJ = 1\,1$, $\frac{1}{2}\,1$ and 01

For the vector channels we find poles corresponding to the $\rho(770)$ and $K^*(892)$. Data are reproduced in a straightforward way, though we have to distinguish between the bare ρ and K^* masses with fitted values given in Eq. (53). The quality of the fit is the same regardless we free their subtraction constants or fix them to the scalar channels. This indicates that unitarity effects are not so important, though they provide the right widths to the bare poles [10]. The masses and widths also agree well with the PDG values [1].

In addition, we have another pole corresponding to the $\phi(1020)$ resonance in the vector isoscalar channel. We obtain a small width for this resonance to two kaons of around 3 MeV, which is close to the experimental partial decay width of the $\phi(1020)$ to this decay channel of 3.5 MeV [1]. Nonetheless, another important decay channel for the $\phi(1020)$ is the $\pi\pi\pi$ state which is not considered in our approach.

5.3 N_C trajectories of the resonance poles

As discussed above in the Introduction, one of the important improvements of our current work is to take into account the N_C dependence of the pseudo-Goldstone boson masses when discussing the N_C trajectories for the resonances. This may potentially cause some significant effects because in the large N_C limit the $U_A(1)$ anomaly disappears and the η' becomes also a pseudo-Goldstone boson [30].

Again we clarify that when fitting our theoretical formulas with the experimental data, all the masses of the pseudo Goldstone bosons are taken from PDG [1], which we summarize in the Appendix E for completeness. Only when discussing the N_C trajectories we start to use our prediction for the pseudo-Goldstone masses. The leading order mass parameters $\overline{m}_\pi = 2Bm_q$ and $\overline{m}_K = B(m_q + m_s)$ in Eq.(1), do not vary with N_C because $B \sim \mathcal{O}(N_C^0)$. This follows from the expression for the quark condensate in the chiral limit from Eq. (1), $\langle 0|\bar{q}^i q^j|0\rangle = -F^2 B\delta^{ij}$, taking into account that both the quark condensate and F^2 are proportional to N_C. The bare masses are fixed in terms of the physical masses of the pion and kaon by employing the expressions given in Eqs. (B.2) and (B.4), with the resulting values

$$\overline{m}_\pi = 139.5^{+4.4}_{-4.6}\ \text{MeV}\,, \qquad \overline{m}_K = 519.6^{+12.0}_{-7.5}\ \text{MeV}\,. \tag{61}$$

We summarize here the N_C scalings of the remaining parameters entering in our equations [36, 44]

$$\begin{aligned} &\Lambda_2 \sim \frac{1}{N_C}\,, \quad M_0 \sim \frac{1}{\sqrt{N_C}}\,, \quad \left\{F_\pi\,, c_d\,, c_m\,, \tilde{c}_d\,, \tilde{c}_m\,, G_V\right\} \sim \sqrt{N_C}\,, \\ &\left\{M_{S_1}\,, M_{S_8}\,, M_\rho\,, M_{K^*}\,, M_\omega\,, M_\phi\,, a_{SL}\right\} \sim \mathcal{O}(1)\,. \end{aligned} \tag{62}$$

As commented above the $U(3)$ large N_C relations between the singlet and octet scalar couplings [44]

$$\tilde{c}_d = \frac{c_d}{\sqrt{3}}\,, \quad \tilde{c}_m = \frac{c_m}{\sqrt{3}}\,, \tag{63}$$

are well fulfilled by our fitted values in Eq. (53), while the mass relation $M_{S_1} = M_{S_8}$ is not.

Our full result for the N_C dependence of the masses for the π Eq. (B.2), K Eq. (B.4), η and η' Eq. (17), as well as the leading order mixing angle θ Eq. (B.7), are shown in Figs. 8 and 9, respectively. The N_C trajectories of poles are displayed in Figs. 10, 11, 12, 13 and 14.

For large N_C all the masses of the pseudo-Goldstone bosons $\pi\,, K\,, \eta$ and η' go to zero in the chiral limit. However, for non-vanishing quark masses the η' meson still gains a relatively large mass in the large N_C limit while the η becomes similarly light as the pion [84]. This can be easily understood by looking at the leading order prediction in the large N_C limit for the pseudoscalar masses,

$$\begin{aligned} \overline{m}_\eta^2 &= \overline{m}_\pi^2\,, \\ \overline{m}_{\eta'}^2 &= 2\overline{m}_K^2 - \overline{m}_\pi^2\,, \end{aligned} \tag{64}$$

where $\overline{m}_\eta$ and $\overline{m}_{\eta'}$ stand for the masses of the η and η' mesons, corresponding to the notations of $m_{\overline{\eta}}$ and $m_{\overline{\eta}'}$ in Eqs.(B.5) and (B.6) with $M_0 \to 0$. Now, taking into account the values given in Eq. (61) for $\overline{m}_\pi$ and $\overline{m}_K$ we then end with the following prediction for the leading order masses of η and η' in the large N_C limit

$$\overline{m}_\eta = 139.5^{+4.4}_{-4.6}\ \text{MeV}\,, \qquad \overline{m}_{\eta'} = 721.5^{+17.4}_{-11.1}\ \text{MeV}\,. \tag{65}$$

This leading order result already explains qualitatively the N_C behaviors for the masses of η and η' mesons shown in Fig. 8.

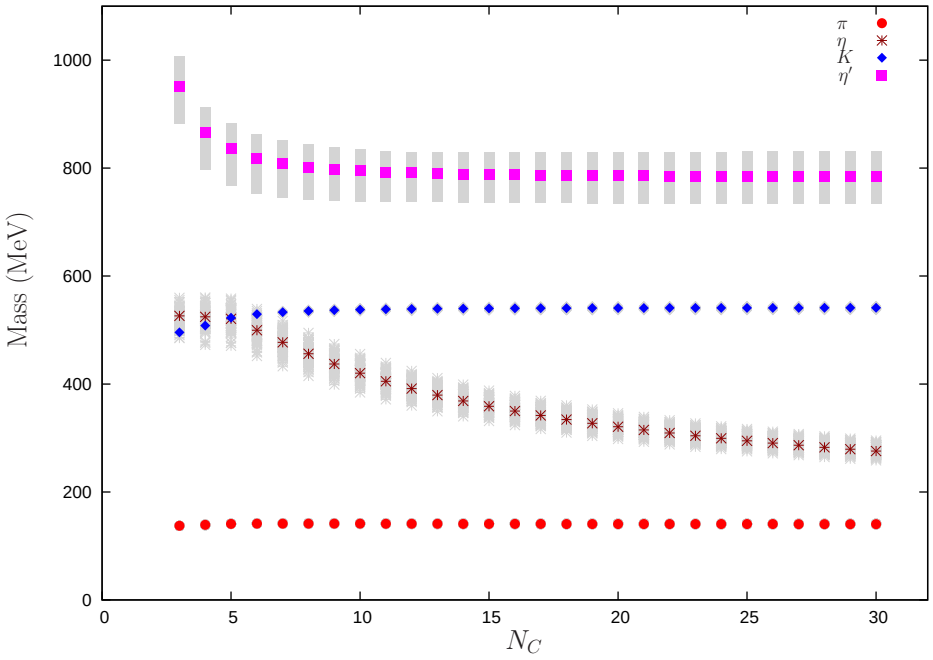

Figure 8: (Color online.) Masses for π, K, η and η' as a function of N_C from 3 to 30 with one unit step. The different points are obtained by using the best fit given in Eq.(53) and the shadowed regions correspond to the error bands. Squares (magenta) are for η', diamonds (blue) for K, bursts (brown) for η and circles (red) for π.

For the leading order mixing angle θ, its N_C dependence is dominantly governed by the $U_A(1)$ anomaly mass M_0, as one can see from Eq.(B.7). It is also easy to demonstrate that in the large N_C limit, i.e. $M_0 = 0$, the leading order mixing of $\eta - \eta'$ turns out to be the ideal mixing: $\theta = -57.7^\circ$, as it should.

One should stress that the previous works discussing the N_C behaviors of resonances, such as Refs.[19, 21], directly identify the η meson with η_8, since it is based on $SU(3)$ χPT. In addition, all of the pseudo-Goldstone masses are not changed in the variation of N_C [19, 20, 21, 40], while as we have just shown the variation with N_C for the η mass is very pronounced.

Next we discuss our findings for the N_C dependence of the resonance properties channel by channel. As a clarifying remark let us mention that the following discussions are based mainly on the resonance poles appearing in the most relevant Riemann sheets for the energy region under discussion, as previously elaborated, unless a specific statement is given.

Poles in the $IJ = 00$ channel

We can easily track the pole trajectories for the σ, $f_0(980)$ and $f_0(1370)$ resonances while varying N_C, which are shown in Figs. 10 and 11.

Concerning σ pole trajectory our full results correspond to the circles shown in Fig. 10. We observe that the width increases very fast with N_C, so that already for $N_C = 7$ it doubles as compared with its value at $N_C = 3$. In regards to its mass it first increases with N_C but for N_C above 7 it decreases. These results are different from those obtained in Ref. [20] by employing the IAM framework with a two loop $SU(2)$ χPT result, where the σ pole falls down to the real axis at 1 GeV, instead of blowing up in the

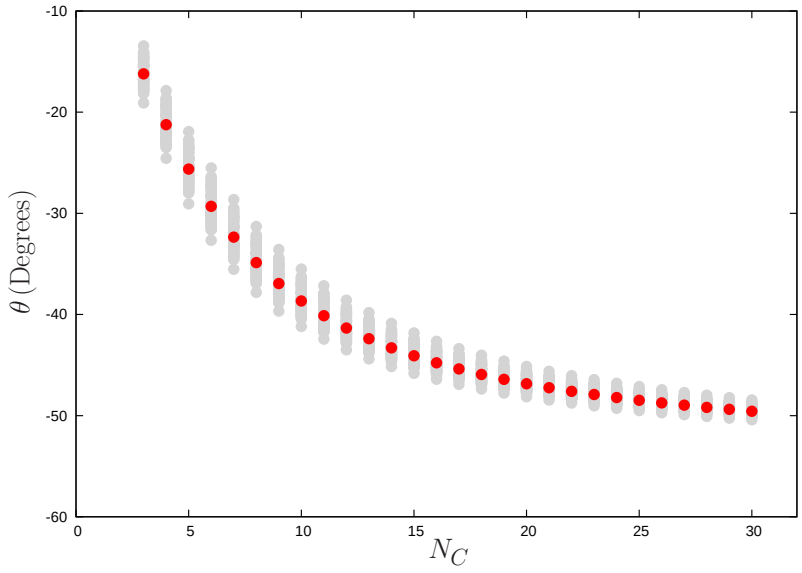

Figure 9: (Color online.) Leading order $\eta - \eta'$ mixing angle θ Eq. (B.7) as a function of N_C from 3 to 30 with one unit step. Similar to Fig. 8, the circle (red) points are from the best fit given in Eq.(53) and the shadowed area corresponds to the error bands.

complex plane as in our case. Indeed, as discussed in more detail below, we also obtain a pole in the large N_C limit at $\sqrt{s} = M_{S_1} \simeq 1$ GeV, but it comes from the bare singlet state which, for $N_C = 3$, is part of the $f_0(980)$ resonance. Compared with the IAM using one loop $SU(3)$ χPT, our result shows a different feature too, as the mass of the σ always increases in the IAM case [19].

It is interesting to point out that we can recover a similar N_C behavior of the σ resonance as that given in Ref. [19] if we freeze out the full propagators of the vector resonances exchanged in the crossed channels and only take the leading local terms generated by them. This in fact corresponds to integrating out the vector resonance states in our theory and keeping only the leading contributions in the low energy sector, which are $\mathcal{O}(p^4)$. These terms are the ones incorporated in the one loop χPT calculation used in [19], but not the higher order ones that arise by keeping the full vector resonance propagators that enter in our full calculation. The corresponding trajectory within this approximation is shown in Fig. 10 by the triangles, labeled as *vector reduced* throughout. Notice that now the mass of the σ keeps increasing with N_C, and the resulting trajectory is quite similar to that obtained in Ref. [19], particularly for $N_C \lesssim 10$. In contrast, to integrate out or keep the full contributions of the bare scalar resonance exchanges from $\mathcal{L}_S$ Eq. (5) does not change the N_C trajectory of σ in a significant way. This is somehow understandable by looking at how the resonances contribute to the LECs in χPT. For example, $L_1\,, L_2$ in $SU(3)$ χPT are purely contributed by the vector resonances, which also dominate L_3 [44]. For $L_4\,, L_5\,, L_6\,, L_8$, they are dominated by the scalar resonances [44]. Precisely in the $\pi\pi \to \pi\pi$ process, the factors accompanying $L_4\,, L_5\,, L_6\,, L_8$ are always proportional to $s\,m_\pi$, $t\,m_\pi$ or m_π^4, which are less important in the resonance region than the terms $L_1\,, L_2\,, L_3$ that are accompanied by s^2, st or t^2.

The N_C trajectory for $f_0(980)$ is not reported in the IAM method due to the difficulty to track this pole [19]. In contrast, in our case its variation when moving N_C can be easily followed. The trajectories of the $f_0(980)$ and $f_0(1370)$ also post a strong evidence that they are originated from the singlet and octet scalar states in the Lagrangian, respectively. However, one should also take into account that the contribution to the physical $f_0(980)$ due to a $K\bar{K}$ bound state [9, 10, 80, 81, 82] disappears in the large

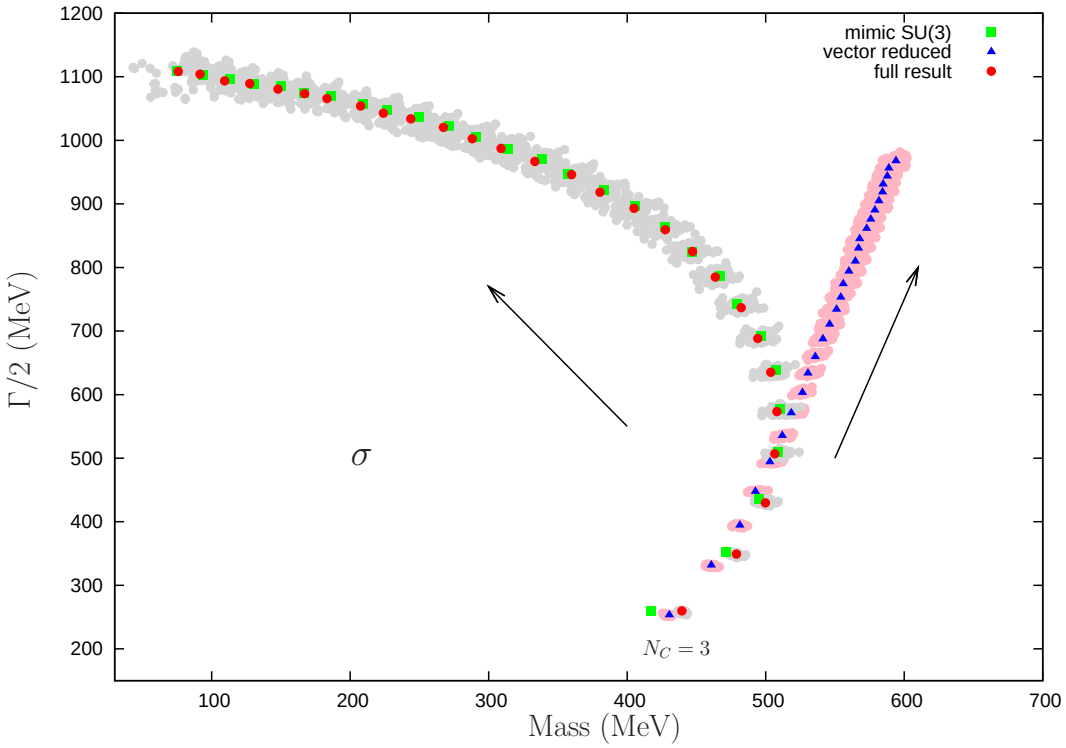

Figure 10: (Color online.) Dependence of the σ pole position, mass and half width, as a function of N_C from 3 to 30 with one unit step. The *full result* (circle in red) corresponds to our calculation without any approximation. The points labeled as *mimic SU(3)* (square in green) and *vector reduced* (triangle in blue) are obtained under some specific amputations of the full result, which are explained in the text. The shadowed area with gray color enveloping the circles shows the error bands of our full result. The shadowed area with pink color around the triangles corresponds to the error bands within the *vector reduced* approximation.

N_C limit.

As one can already see from the Table 1, the channels involving η and η' mesons have larger coupling strengths to the $f_0(980)$ and $f_0(1370)$ resonances, albeit they are weakly coupled to σ. As a result one should expect larger effects associated to these channels on the $f_0(980)$ and $f_0(1370)$ resonances than on the σ. Compared with $SU(3)$ χPT, where η is identified with the octet η_8 and η_1 is only implicitly included through the LEC L_7, the present discussion incorporates the explicit contributions from the physical states of η and η' within $U(3)$ χPT with the δ counting. Thus, it is interesting to find a way to make closer our approach to the $SU(3)$ ones and then compare. This can be achieved by imposing the following conditions when varying N_C: i) Freezing the mixing angle θ at leading order in Eq.(12) to zero, together with the higher order mixing parameters in Eq.(13). ii) The masses of the η (then η_8), $\pi\,, K$ are fixed to their physical values and do not vary with N_C. iii) The η_1 mass is also fixed by using the leading order result from Eq.(1) without mixing, which gives the value 1040 MeV. In this way, the η meson in $U(3)$ χPT resembles the η_8 in $SU(3)$ χPT and the η_1 only appears in the scattering amplitudes involving $\pi\,, K\,, \eta$ mesons through the loops, which is suppressed by $1/N_C$. This mimics the role of L_7 in $SU(3)$ χPT [19], although one needs to be careful about the N_C counting for L_7 [85]. The corresponding N_C trajectories within this approximation, named as *mimic SU(3)* throughout, are shown in Figs. 10 and 11, by the square points. Since the main difference between the approximation *mimic SU(3)* and the

full result is the treatment of the η and η' mesons, by comparing the results from these two frameworks one can test the role of η' in determining the properties of resonances. We see that the difference in the trajectories obtained in the full result and *mimic SU(3)* cases differ significantly for the $f_0(980)$ and $f_0(1370)$ resonances, while the change is almost negligible for the σ. This is expected because the σ couples only marginally to any channel including η or η', as shown in Table 1. This fact is kept when varying N_C as we have explicitly checked, even though the η mass decreases significantly with N_C.

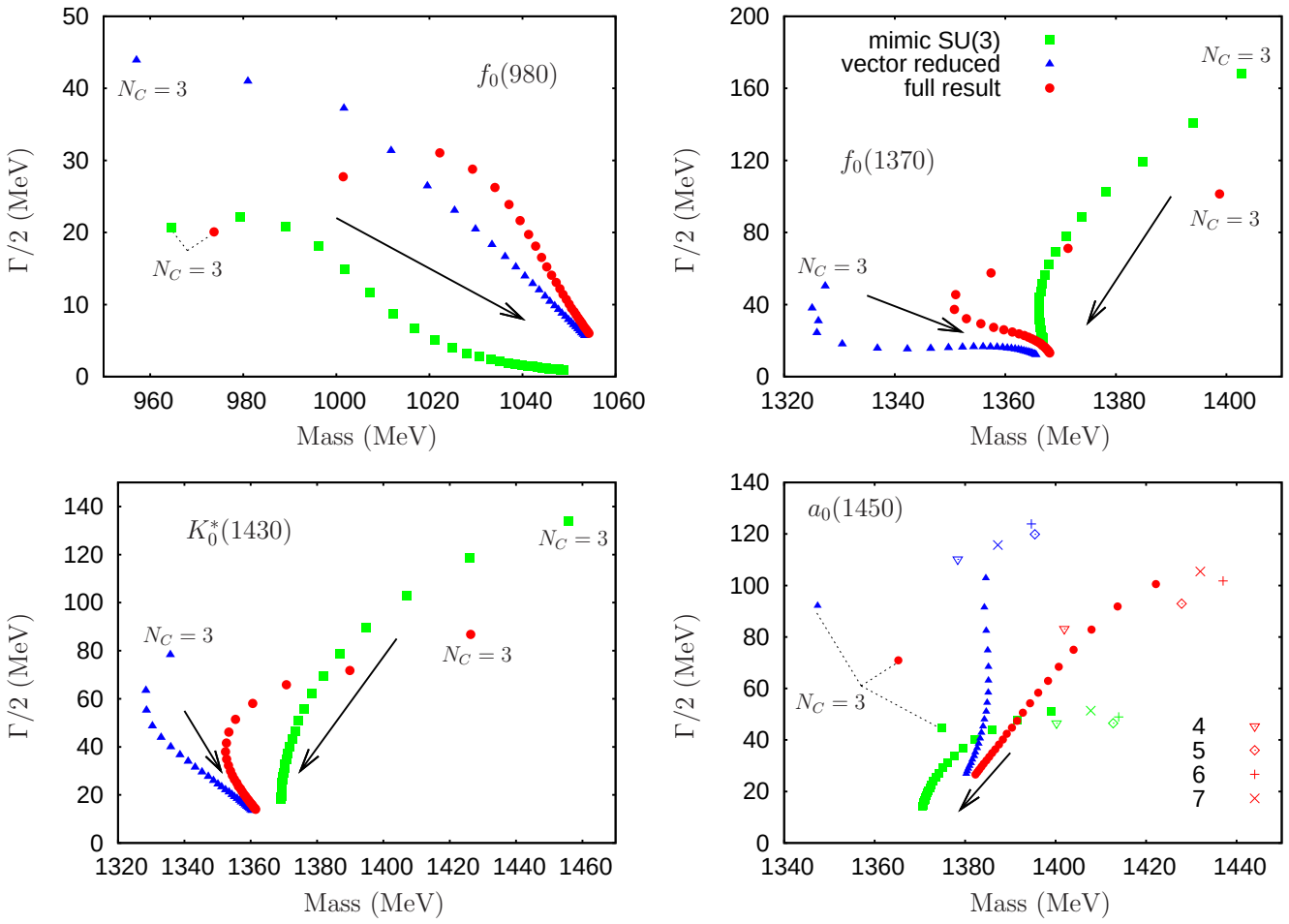

Figure 11: (Color online.) From top to bottom and left to right: Dependence on N_C from 3 to 30 with one unit step for the pole positions of the $f_0(908)$, $f_0(1370)$, $K_0^*(1430)$ and $a_0(1450)$, respectively. The notation is the same as that in Fig. 10. For the last panel dedicated to the $a_0(1450)$ the N_C points for $N_C \leq 7$ are indicated explicitly for clarifying purposes. All the points with the same color correspond to the same framework.

To further test the stability of the N_C behavior of the σ resonance, we use the same configurations of parameters that we exploit before in calculating the error bands from our fits in Eq. (53) and in Figs. 5-7. In this way we obtain the error bands for the N_C trajectories of the σ in Fig. 10. As one can see from this figure our conclusions for the σ are quite stable even after taking into account the uncertainties of the inputs. For $f_0(980)$ and $f_0(1370)$, since in our case their poles always fall down to the real axis to

the bare resonances in the Lagrangian, we only show for them the pole trajectories from the best fit in Fig. 11. For $N_C \to \infty$ the uncertainty is already given because their pole positions correspond to the bare masses of the singlet and octet scalar resonances, in order, given in Eq. (53) together with their errors.

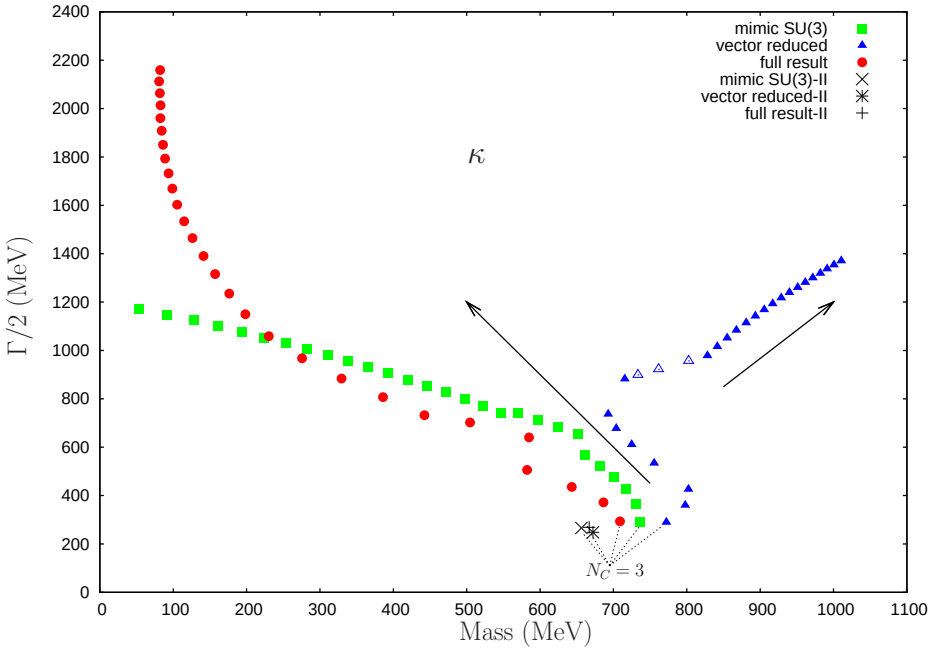

Figure 12: (Color online.) N_C dependence of the κ pole position in the fourth Riemann sheet $(+,-,+)$ from $N_C = 3$ to 30 with one unit step. The notation is the same as in Fig. 10. For $N_C = 3$, the poles in the second Riemann sheet $(-,+,+)$ are also shown by the plus for the full result and by the cross and burst for the *mimic SU(3)* and *vector reduced* approximations, in order. See the text for further details.

From Figs. 10, one can learn a clear lesson: different frameworks could give similar results at the physical point ($N_C = 3$) for σ but providing very different N_C trajectories for the σ pole position because of higher orders in the chiral expansion (differences between the full and *vector reduced* cases.) In addition, one can also learn that different treatments of η and η' barely affect the σ pole position for all values of N_C.

Poles in the $IJ = \frac{1}{2}0$ channel

The $K_0^*(1430)$ pole can be easily tracked in the complex plane, which we show in the third panel of Fig.(11). Like the $f_0(1370)$, this pole falls down on the real axis for $N_C \to \infty$, at $s = M_{S_8}^2$, indicating that it originates from the bare octet scalar states with $I = 1/2$. At $N_C = 3$, its pole is somewhat sensitive to the different modifications of our results already discussed, while for large N_C they run towards to the same point, as expected. From Table 1 we can see that the $K_0^*(1430)$ resonance couples to $K\eta'$ as strongly as to $K\pi$ for $N_C = 3$, while its coupling to $K\eta$ is suppressed. This behavior is also kept when varying N_C.

For the κ pole, the situation is more involved. After $N_C = 4$, we could not find its pole in the second Riemann sheet. However, switching to the fourth sheet, i.e. with $(+,-,+)$, we can then track the κ pole for any value of N_C. As shown above the pole in the sheet $(+,-,+)$ is very similar to that in the $(-,+,+)$

sheet for $N_C = 3$. The resulting trajectory in the fourth Riemann sheet is then shown by the circle points in Fig. 12. Similarly to the σ resonance, it shows quite an interesting feature: for the full result as well as for the *mimic SU(3)* approximation, the κ poles go to the left direction in the complex plane, i.e. with a decreasing mass as N_C increases, while in the *vector reduced* approximation the trajectory tends to the right, i.e. with an increasing mass by increasing N_C. Due to the more complicated cut structures in $IJ = \frac{1}{2}0$ case the trajectories of κ are not as smooth as for the σ in the $IJ = 00$ case. This is the reason why the κ pole in the second Riemann sheet cannot be tracked because at $N_C = 5$ the pole moves to another Riemann sheet obtained by crossing the new cut in the complex plane, so that only a bump remains in the second Riemann sheet. The empty triangles for $N_C = 11$, 12 and 13 in Fig. 12 apply only to the *vector reduced* case and correspond to values of N_C where no κ pole is found, but only bumps appear.

Poles in the $IJ = 10$ channel

The trajectories for the $a_0(1450)$ pole position are shown in the last panel of Fig. 11. One can see that for this resonance the trajectories bend and make a knot for $N_C < 7$. In order to visualize this behavior different symbols for the pole positions up to $N_C = 7$ have been used in the figure. Independently from this peculiar behavior the $a_0(1450)$ pole position trajectories can be followed easily in a smooth way as N_C varies. As expected, for large N_C this pole moves to the real axis with zero width at $s = M_{S_8}^2$, the same position as for the $f_0(1370)$ and $K_0^*(1430)$. It corresponds to the bare isovector members of the scalar octet S_8 Eq. (7). All $SU(3)$ breaking effects in the masses of these heavier scalar resonances originate through pseudoscalar loops and disappear in the large N_C limit.

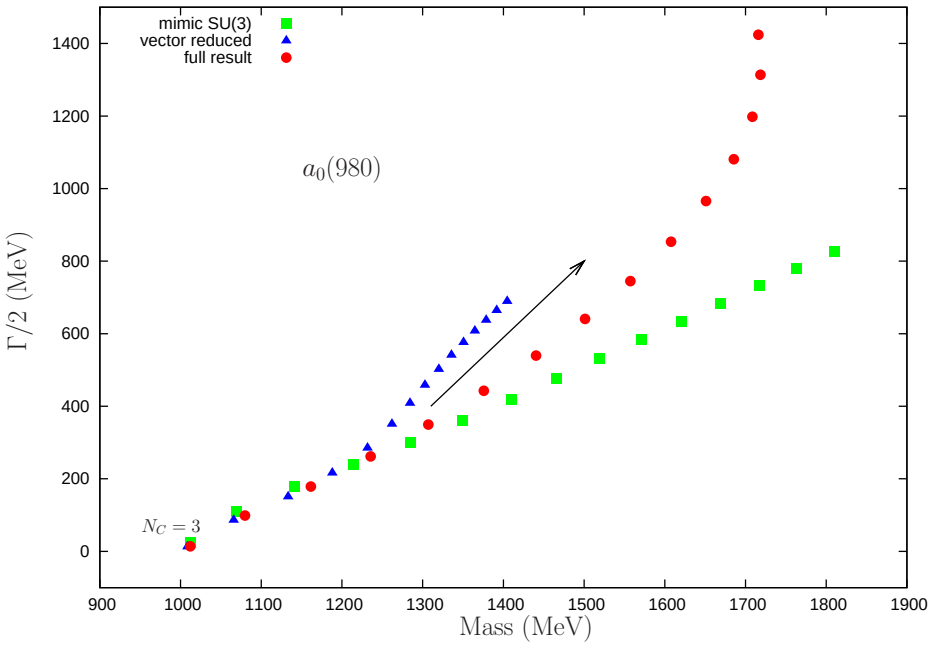

Figure 13: (Color online.) Dependence on N_C for the $a_0(980)$ pole position from 3 to 17 with one unit step. The notation is the same as in Fig. 10.

For the $a_0(980)$ pole in the fourth sheet, we can track its trajectory up to $N_C = 17$ without any difficulty, which we display in Fig.(13). After $N_C = 18$, only bumps appear in this sheet because there

is a cut in the complex plane that connects the fourth Riemann sheet with another one, that would be obtained by crossing continuously this cut in the complex plane (not the real axis on which the standard Riemann sheets based on unitarity are defined), where the pole is finally located. Contrary to the κ case we cannot find a unique sheet where we can track the pole position from $N_C = 3$ onwards to high values of N_C. Although similar poles can be tracked if we switch to other sheets for $N_C > 17$, there is some discontinuity when passing from one trajectory to another in different Riemann sheets. The trajectory shown in Fig. 13 corresponding to our full results clearly indicates that this resonance is dynamically generated [82, 9, 10], since it moves further and further in the complex plane with a huge width increasing very fast with N_C.

Poles in the $IJ = 11$, $\frac{1}{2}1$ and 01 channels

The N_C trajectories of the $\rho(770)$ and $K^*(892)$ vector resonances are shown in the left and right panels, respectively, of Fig. 14. Both the ρ and K^* move to the real axis with increasing N_C, as one can see in Fig.(14), indicating that their widths vanish in large N_C limit. Indeed they vanish exactly as $1/N_C$. In addition their masses move very little. Both facts are in agreement with its standard interpretation as $\bar{q}q$ resonances which implies an N_C^0 scaling with N_C for the mass and $1/N_C$ for the width.

Our results agree well with the previous conclusions on this respect [19, 20]. Nevertheless, the N_C trajectories of the residues for the $K^*(892)$ in our full calculation show a clearly different feature, compared with the *mimic SU(3)* approximation. As one can see in Fig. 15, the residues of $K\pi$ are rather similar between the two frameworks, while the residues of $K\eta'$ in the full result are obviously larger than the $K\eta_1$ in the *mimic SU(3)* approximation, which can be attributed to the $\eta - \eta'$ mixing angle. In contrast to the almost flat residue of $K\eta$ (in fact $K\eta_8$) in *mimic SU(3)* approximation, a more complicated structure appears in the full result. We verify this structure is caused by the N_C variation of the η mass. As one can see the kink in the residue of $K\eta$ happens around $N_C = 14$, where precisely the $K\eta$ threshold starts to be lower than the $K^*(892)$ mass.

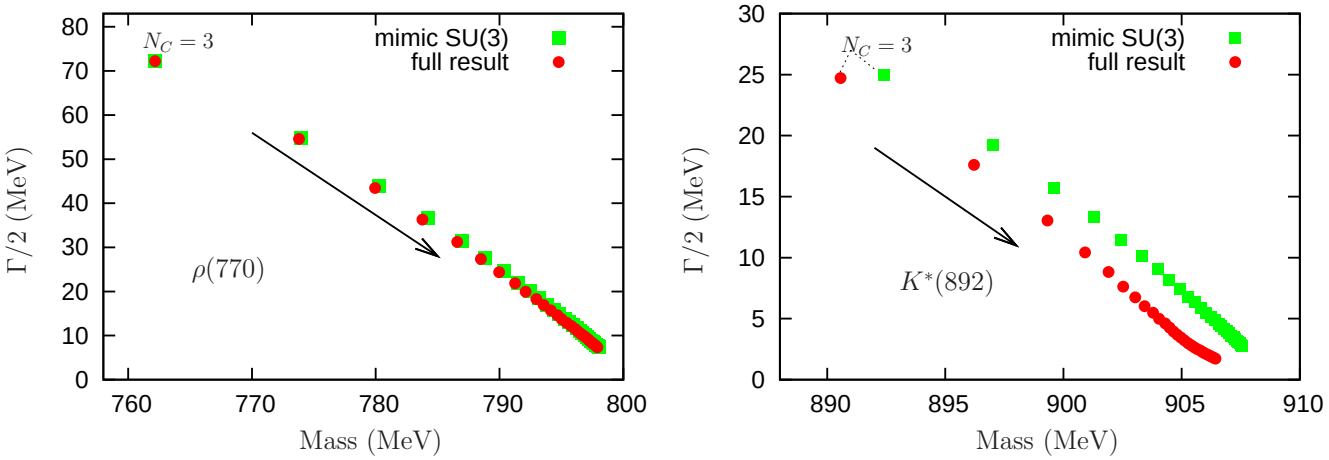

Figure 14: (Color online.) Dependence on N_C of the $\rho(770)$ and $K^*(892)$ pole positions as a function of N_C from 3 to 30 with one unit step. The notation is the same as in Fig. 10, though in this case we do not show the *vector reduced* trajectory for obvious reasons.

The N_C trajectory for the $\phi(1020)$ pole position is completely analogous to those discussed for the

$\rho(770)$ and $K^*(892)$, but even simpler because the width of the $\phi(1020)$ is very small, Table 1. This is why we do not dedicate a separate figure for this case. This type of trajectory is then in agreement with the standard $\bar{q}q$ interpretation for this resonance. Nevertheless, there is some movement in the $\phi(1020)$ mass due to the small variation of the nearby $K\bar{K}$ threshold with N_C, see Fig. 8.

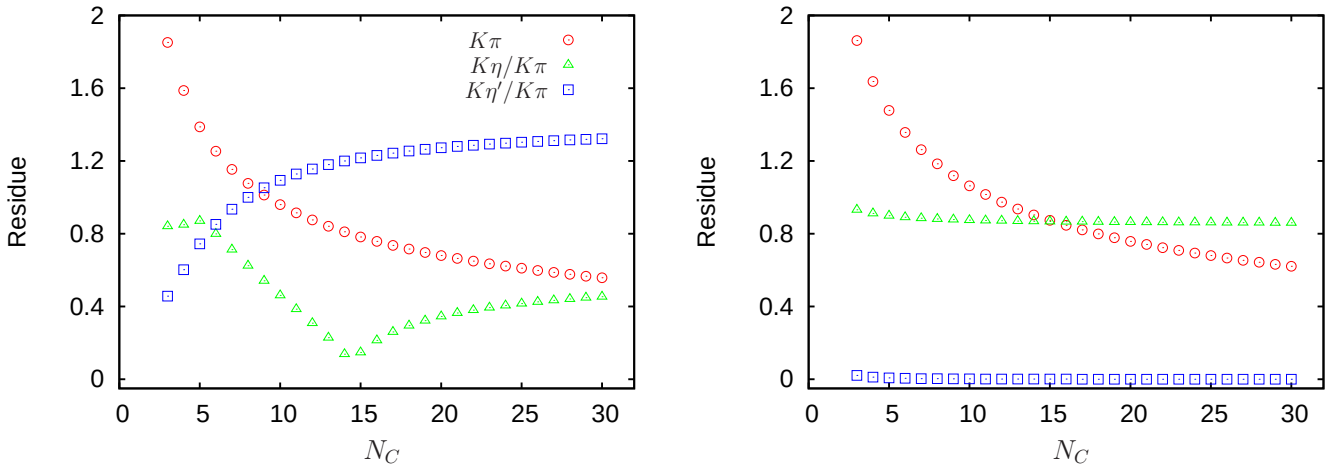

Figure 15: (Color online.) The N_C running of the various residues of the $K^*(892)$ resonance. The absolute value of the coupling to $K\pi$ is given by the circular points, while for the other states the ratio to the $K\pi$ coupling is shown. Triangles apply to $K\eta$ ($K\eta_8$) and squares to $K\eta'$ ($K\eta_1$). The left (right) panel corresponds to our full (*mimic SU(3)*) results.

6 Conclusions

In this work, we complete the first one-loop calculation of meson-meson scattering in $U(3)$ χPT in the literature. It is also the first work in which the N_C trajectories of resonance pole positions are studied taking into account the fact that the η_1 becomes the ninth Goldstone boson in the large N_C limit.

In our one-loop $U(3)$ χPT calculation instead of the local terms at $\mathcal{O}(\delta^3)$ we include explicit resonance fields whose exchange generates these terms, as well as higher order ones. In order to compare with data, including the resonance region, we have unitarized the previous one-loop amplitudes projected in partial waves. For the unitarization we employ a non-perturbative scheme based on the N/D method, where the right-hand cut is resummed while the crossed-channel cuts are perturbatively treated as given by the input partial waves from $U(3)$ χPT. We achieve a good reproduction of meson-meson scattering data from $\pi\pi$ threshold up to energies between 1.2-1.6 GeV, depending on the particular partial wave.

We have then studied the spectroscopy content of our solution by considering the poles and related residues of the different partial waves. Various resonance poles in the complex energy plane are then found, namely, for the σ, $f_0(980)$, $f_0(1370)$, κ, $K_0^*(1430)$, $a_0(980)$, $a_0(1450)$, $\rho(770)$, $K^*(892)$ and $\phi(1020)$ resonances. The pole positions agree remarkably well with the PDG values [1]. The corresponding residues are calculated as well, which give us the coupling strengths of every resonance to the different channels with the same quantum numbers taken in our study.

We pay special attention to the N_C dependences of the poles for these resonances as well as for their residues. Our approach is specially suited for this aim because previous studies in the literature did not take into account the Goldstone boson nature of the η_1 field in the large N_C limit, due to the vanishing of the $U_A(1)$ anomaly with large N_C. The trajectories for the pole positions are obtained by properly

scaling with N_C the pion decay constant, the $U_A(1)$ anomaly mass and the bare resonance parameters. The N_C dependences of the pseudo-Goldstone masses have been taken into account for determining the resulting trajectories. It is specially remarkable the large reduction of the η mass with N_C, that becomes similarly light as the pion for large N_C. We also find that higher order terms arising within our approach by keeping the full resonance propagators in the crossed vector resonance exchanges give rise to a qualitative different behavior in many resonance pole position trajectories, as found for the σ and κ cases for not too large N_C values ($N_C \gtrsim 7$). This is easily understood because for increasing N_C the loop contributions from crossed diagrams tend to vanish faster with N_C than those from the resonance exchange diagrams. In this way, the cancellation between both contributions found in Ref. [10] at $N_C = 3$ for the resonant scalar channels below 1 GeV, is spoilt for higher values of N_C and then there is more sensitivity to crossed channel dynamics. As a result, we find that the pole positions for the σ and κ resonances have a mass that typically decreases with N_C, while this is not the case if the vector resonance exchanges are reduced to the leading local term contribution as in previous studies.

Regarding the $f_0(980)$ we conclude that in the large N_C limit it tends to a zero width pole position corresponding to the bare singlet scalar resonance around 1 GeV. It is worth stressing that in other studies a zero width pole with mass of 1 GeV was already found for large N_C from the evolution of the σ pole trajectory. However, the pole at 1 GeV disappears in those studies for $N_C = 3$ and only the σ remains [20]. In our case, both states remain. On the one hand, we have the bare scalar pole around 1 GeV that contributes to the $f_0(980)$ resonance pole in $N_C = 3$ while, on the other hand, the σ resonance originates dynamically mainly from pion interactions. In addition, the strong $K\bar{K}$ interactions near threshold in S-wave gives rise to another strong contribution to the $f_0(980)$ as a $K\bar{K}$ bound state. This contribution disappears in the large N_C limit and only the bare singlet scalar state pole contributes then. We also discuss the N_C trajectories for the $f_0(1370)$, $a_0(1450)$ and $K^*(1430)$. Asymptotically for large N_C, they tend to the zero width pole position of the bare octet of scalar resonances included at the tree-level around 1.4 GeV. The $a_0(980)$ resonance disappears deep in the complex plane for large N_C, similarly as the σ and κ, as it corresponds to a dynamically generated resonance.

Finally, the vector resonances $\rho(770)$, $K^*(892)$ and $\phi(1020)$ are reproduced with properties in good agreement with the PDG [1]. They have a N_C pole position trajectory in good agreement with the expectations for a $\bar{q}q$ state, with a quenched mass running as N_C^0 and the width decreasing as $1/N_C$. The decreasing η mass with N_C makes that the $K^*(892)$ resonance becomes heavier than the $K\eta$ channel for N_C around 15. The crossover between the mass of the resonance and the $K\eta$ threshold manifests in a kink in the coupling to $K\eta$.

Acknowledgement

We would like to dedicate this work to Joaquim Prades who passed away while this work was being done. He encouraged us to get involved in this research and also collaborated in an earlier stage of the work. We also thank Miguel Albaladejo for technical assistance with computer software and Felipe Llanes for discussions. This work is partially funded by the grants FPA2010-17806 and the Fundación Séneca one Ref. 11871/PI/09. Financial support from the EU-Research Infrastructure Integrating Activity "Study of Strongly Interacting Matter" (HadronPhysics2, grant n. 227431) under the Seventh Framework Program of EU and the Consolider-Ingenio 2010 Programme CPAN (CSD2007-00042) is also acknowledged. Z.H.G. acknowledges CPAN postdoc contract in the Universidad de Murcia and financial support from the grants Natural Science Foundation of Hebei Province with contract No. A2011205093 and Doctor Foundation of Hebei Normal University with contract No. L2010B04.

Appendix

A Convention of the loop functions

The one-loop functions that appear in our $U(3)$ χPT calculation are calculated in dimensional regularization within the $\overline{MS}-1$ renormalization scheme [25]. They are defined as

$$\begin{aligned} A_0(m^2) &= \frac{(2\pi\mu)^{4-D}}{i\pi^2}\int d^Dq\,\frac{1}{q^2-m^2} \\ &= -m^2\ln\frac{m^2}{\mu^2}\,, \\ B_0(s,m_a^2,m_b^2) &= \frac{(2\pi\mu)^{4-D}}{i\pi^2}\int d^Dq\,\frac{1}{q^2-m_a^2}\frac{1}{(q-p)^2-m_b^2} \\ &= 1-\log\frac{m_b^2}{\mu^2}+x_+\log\frac{x_+-1}{x_+}+x_-\log\frac{x_--1}{x_-}\,, \end{aligned} \tag{A.1}$$

where μ is the renormalization scale, $s=p^2$ and $x_\pm$ was defined in Eq.(32). In case of equal masses, the two-point function reduces to

$$B_0(s,m^2) = 1-\log\frac{m^2}{\mu^2}+\sigma(s)\log\frac{\sigma(s)-1}{\sigma(s)+1}\,, \tag{A.2}$$

with $\sigma(s)$ defined in Eq. (34).

B Renormalization of the wave functions and masses

From the calculation of the π, K, $\overline{\eta}$ and $\overline{\eta}'$ self-energies Fig. 3, with the latter fields defined in Eq. (12), we have:

$$Z_\pi = 1-\frac{1}{16\pi^2F_\pi^2}\left[\frac{2}{3}A_0(m_\pi^2)+\frac{1}{3}A_0(m_K^2)\right]+\left[-\frac{8\widetilde{c}_d\,\widetilde{c}_m(2m_K^2+m_\pi^2)}{F_\pi^2M_{S_1}^2}+\frac{16c_d\,c_m(m_K^2-m_\pi^2)}{3F_\pi^2M_{S_8}^2}\right], \tag{B.1}$$

$$\begin{aligned} m_\pi^2 = \overline{m}_\pi^2 &- \frac{1}{16\pi^2F_\pi^2}\left[\frac{m_\pi^2}{2}A_0(m_\pi^2)-\frac{m_\pi^2(c_\theta-\sqrt{2}s_\theta)^2}{6}A_0(m_\eta^2)-\frac{m_\pi^2(\sqrt{2}c_\theta+s_\theta)^2}{6}A_0(m_{\eta'}^2)\right] \\ &+\left[\frac{8\widetilde{c}_m(\widetilde{c}_m-\widetilde{c}_d)\,m_\pi^2(2m_K^2+m_\pi^2)}{F_\pi^2M_{S_1}^2}-\frac{16c_m(c_m-c_d)\,m_\pi^2(m_K^2-m_\pi^2)}{3F_\pi^2M_{S_8}^2}\right], \end{aligned} \tag{B.2}$$

$$\begin{aligned} Z_K = 1 &- \frac{1}{16\pi^2F_\pi^2}\left[\frac{1}{4}A_0(m_\pi^2)+\frac{1}{2}A_0(m_K^2)+\frac{c_\theta^2}{4}A_0(m_\eta^2)+\frac{s_\theta^2}{4}A_0(m_{\eta'}^2)\right] \\ &+\left[-\frac{8\widetilde{c}_d\,\widetilde{c}_m(2m_K^2+m_\pi^2)}{F_\pi^2M_{S_1}^2}-\frac{8c_d\,c_m(m_K^2-m_\pi^2)}{3F_\pi^2M_{S_8}^2}\right], \end{aligned} \tag{B.3}$$

$$
\begin{aligned}
m_K^2 = \overline{m}_K^2 - \frac{1}{16\pi^2 F_\pi^2}\Bigg[& \frac{c_\theta^2(3m_\eta^2+m_\pi^2)+2\sqrt{2}c_\theta s_\theta(m_\pi^2-2m_K^2)-4s_\theta^2 m_K^2}{12}A_0(m_\eta^2) \\
& + \frac{-4c_\theta^2 m_K^2+2\sqrt{2}c_\theta s_\theta(2m_K^2-m_\pi^2)+s_\theta^2(3m_{\eta'}^2+m_\pi^2)}{12}A_0(m_{\eta'}^2)\Bigg] \\
& + \left[\frac{8\widetilde{c}_m(\widetilde{c}_m-\widetilde{c}_d)\,m_K^2(2m_K^2+m_\pi^2)}{F_\pi^2 M_{S_1}^2} + \frac{8c_m(c_m-c_d)\,m_K^2(m_K^2-m_\pi^2)}{3F_\pi^2 M_{S_8}^2}\right], \qquad \text{(B.4)}
\end{aligned}
$$

The leading order masses of $\overline{\eta}\,,\overline{\eta}'$, i.e. $m_{\overline{\eta}}$ and $m_{\overline{\eta}'}$ defined in Eq.(13), and the $\overline{\eta}-\overline{\eta}'$ mixing angle from Eq.(1) are found to be

$$
\begin{aligned}
m_{\overline{\eta}}^2 &= \frac{M_0^2}{2}+\overline{m}_K^2-\frac{\sqrt{M_0^4-\frac{4M_0^2\Delta^2}{3}+4\Delta^2}}{2}\,, & \text{(B.5)}\\
m_{\overline{\eta}'}^2 &= \frac{M_0^2}{2}+\overline{m}_K^2+\frac{\sqrt{M_0^4-\frac{4M_0^2\Delta^2}{3}+4\Delta^2}}{2}\,, & \text{(B.6)}\\
\sin\theta &= -\left(\sqrt{1+\frac{\left(3M_0^2-2\Delta^2+\sqrt{9M_0^4-12M_0^2\Delta^2+36\Delta^4}\right)^2}{32\Delta^4}}\right)^{-1}\,, & \text{(B.7)}
\end{aligned}
$$

with $\Delta^2=\overline{m}_K^2-\overline{m}_\pi^2$.

The higher order mixing parameters of $\overline{\eta}-\overline{\eta}'$ are defined in Eq.(13). They read

$$
\begin{aligned}
\delta_{\overline{\eta}} &= \frac{c_\theta^2}{16\pi^2F_\pi^2}A_0(m_K^2)-\left[-\frac{8\widetilde{c}_m\widetilde{c}_d\,(2m_K^2+m_\pi^2)}{F_\pi^2M_{S_1}^2}-\frac{16c_mc_d\,(m_K^2-m_\pi^2)(c_\theta^2+2\sqrt{2}c_\theta s_\theta)}{3F_\pi^2M_{S_8}^2}\right],\\
\delta_{\overline{\eta}'} &= \frac{s_\theta^2}{16\pi^2F_\pi^2}A_0(m_K^2)-\left[-\frac{8\widetilde{c}_m\widetilde{c}_d\,(2m_K^2+m_\pi^2)}{F_\pi^2M_{S_1}^2}-\frac{16c_mc_d\,(m_K^2-m_\pi^2)(s_\theta^2-2\sqrt{2}c_\theta s_\theta)}{3F_\pi^2M_{S_8}^2}\right],\\
\delta_k &= \frac{s_\theta c_\theta}{16\pi^2F_\pi^2}A_0(m_K^2)+\frac{16c_d\,c_m\,(m_K^2-m_\pi^2)(\sqrt{2}s_\theta^2+c_\theta s_\theta-\sqrt{2}c_\theta^2)}{3F_\pi^2M_{S_8}^2}\,,\\
\delta_{m_{\overline{\eta}}^2} &= -\frac{1}{16\pi^2F_\pi^2}\Bigg\{-\frac{m_\pi^2(c_\theta-\sqrt{2}s_\theta)^2}{2}A_0(m_\pi^2)\\
&\quad+\frac{c_\theta^2m_\pi^2+2\sqrt{2}c_\theta s_\theta(m_\pi^2-2m_K^2)-4s_\theta^2m_K^2}{3}A_0(m_K^2)\\
&\quad-\frac{A_0(m_\eta^2)}{18}\Big[c_\theta^4(16m_K^2-7m_\pi^2)+4\sqrt{2}c_\theta^3s_\theta(8m_K^2-5m_\pi^2)\\
&\qquad+12c_\theta^2s_\theta^2(4m_K^2-m_\pi^2)+16\sqrt{2}c_\theta s_\theta^3(m_K^2-m_\pi^2)+2s_\theta^4(2m_K^2+m_\pi^2)\Big]\\
&\quad-\frac{(4m_K^2-m_\pi^2)(2c_\theta^4-2\sqrt{2}c_\theta^3s_\theta-3c_\theta^2s_\theta^2+2\sqrt{2}c_\theta s_\theta^3+2s_\theta^4)}{18}A_0(m_{\eta'}^2)\Bigg\}\\
&\quad+\left\{\frac{8\widetilde{c}_m^2\,(2m_K^2+m_\pi^2)\left[c_\theta^2(4m_K^2-m_\pi^2)+4\sqrt{2}c_\theta s_\theta(m_K^2-m_\pi^2)+s_\theta^2(2m_K^2+m_\pi^2)\right]}{3F_\pi^2M_{S_1}^2}\right.
\end{aligned}
$$

$$
\begin{aligned}
&+\frac{16\,c_m^2\,(m_K^2-m_\pi^2)\left[c_\theta^2(8m_K^2-5m_\pi^2)+2\sqrt{2}c_\theta s_\theta(4m_K^2-m_\pi^2)+4s_\theta^2(m_K^2-m_\pi^2)\right]}{9F_\pi^2M_{S_8}^2}\Bigg\}\\
&+\frac{2}{3}\Lambda_2\left[2\sqrt{2}s_\theta c_\theta(m_K^2-m_\pi^2)+s_\theta^2(2m_K^2+m_\pi^2)\right],\\
\delta_{m_{\eta'}^2}=&-\frac{1}{16\pi^2F_\pi^2}\Bigg\{-\frac{m_\pi^2(\sqrt{2}c_\theta+s_\theta)^2}{2}A_0(m_\pi^2)\\
&+\frac{-4c_\theta^2m_K^2+2\sqrt{2}c_\theta s_\theta(2m_K^2-m_\pi^2)+s_\theta^2m_\pi^2}{3}A_0(m_K^2)\\
&-\frac{(4m_K^2-m_\pi^2)(2c_\theta^4-2\sqrt{2}c_\theta^3s_\theta-3c_\theta^2s_\theta^2+2\sqrt{2}c_\theta s_\theta^3+2s_\theta^4)}{18}A_0(m_\eta^2)\\
&-\frac{A_0(m_{\eta'}^2)}{18}\Bigg[2c_\theta^4(2m_K^2+m_\pi^2)-16\sqrt{2}c_\theta^3s_\theta(m_K^2-m_\pi^2)\\
&\quad+12c_\theta^2s_\theta^2(4m_K^2-m_\pi^2)-4\sqrt{2}c_\theta s_\theta^3(8m_K^2-5m_\pi^2)+s_\theta^4(16m_K^2-7m_\pi^2)\Bigg]\Bigg\}\\
&+\Bigg\{\frac{8\widetilde{c}_m^2\,(2m_K^2+m_\pi^2)\left[s_\theta^2(4m_K^2-m_\pi^2)-4\sqrt{2}c_\theta s_\theta(m_K^2-m_\pi^2)+c_\theta^2(2m_K^2+m_\pi^2)\right]}{3F_\pi^2M_{S_1}^2}\\
&+\frac{16\,c_m^2\,(m_K^2-m_\pi^2)\left[s_\theta^2(8m_K^2-5m_\pi^2)-2\sqrt{2}c_\theta s_\theta(4m_K^2-m_\pi^2)+4c_\theta^2(m_K^2-m_\pi^2)\right]}{9F_\pi^2M_{S_8}^2}\Bigg\}\\
&+\frac{2}{3}\Lambda_2\Big[-2\sqrt{2}s_\theta c_\theta(m_K^2-m_\pi^2)+c_\theta^2(2m_K^2+m_\pi^2)\Big],\\
\delta_{m^2}=&-\frac{1}{16\pi^2F_\pi^2}\Bigg\{-\frac{m_\pi^2(\sqrt{2}c_\theta^2-c_\theta s_\theta-\sqrt{2}s_\theta^2)}{2}A_0(m_\pi^2)\\
&+\frac{\sqrt{2}c_\theta^2(2m_K^2-m_\pi^2)+c_\theta s_\theta(4m_K^2+m_\pi^2)-\sqrt{2}s_\theta^2(2m_K^2-m_\pi^2)}{3}A_0(m_K^2)\\
&+\frac{A_0(m_\eta^2)}{18}\Bigg[\sqrt{2}c_\theta^4(8m_K^2-5m_\pi^2)+c_\theta^3s_\theta(8m_K^2+m_\pi^2)\\
&\quad+3\sqrt{2}c_\theta^2s_\theta^2(m_\pi^2-4m_K^2)+4c_\theta s_\theta^3(2m_\pi^2-5m_K^2)+4\sqrt{2}s_\theta^4(m_\pi^2-m_K^2)\Bigg]\\
&+\frac{A_0(m_{\eta'}^2)}{18}\Bigg[4\sqrt{2}c_\theta^4(m_K^2-m_\pi^2)+4c_\theta^3s_\theta(-5m_K^2+2m_\pi^2)\\
&\quad+3\sqrt{2}c_\theta^2s_\theta^2(4m_K^2-m_\pi^2)+c_\theta s_\theta^3(m_\pi^2+8m_K^2)+\sqrt{2}s_\theta^4(5m_\pi^2-8m_K^2)\Bigg]\Bigg\}\\
&+\Bigg\{\frac{16c_m^2\,(m_K^2-m_\pi^2)\,(4m_K^2-m_\pi^2)(\sqrt{2}s_\theta^2+c_\theta s_\theta-\sqrt{2}c_\theta^2)}{9F_\pi^2M_{S_8}^2}\\
&-\frac{16\widetilde{c}_m^2\,(m_K^2-m_\pi^2)\,(2m_K^2+m_\pi^2)(\sqrt{2}c_\theta^2-c_\theta s_\theta-\sqrt{2}s_\theta^2)}{3F_\pi^2M_{S_1}^2}\Bigg\}\\
&-\frac{2}{3}\Lambda_2\Big[\sqrt{2}c_\theta^2(m_K^2-m_\pi^2)+s_\theta c_\theta(2m_K^2+m_\pi^2)-\sqrt{2}s_\theta^2(m_K^2-m_\pi^2)\Big]. \qquad \text{(B.8)}
\end{aligned}
$$

C Renormalization of pion decay constant

The definition of pseudoscalar weak decay constant is

$$\langle 0|A_\mu^a|\phi^b(p)\rangle = iF_{\phi^b}\, p_\mu\, \delta^{ab}\,, \tag{C.1}$$

where the axial-vector current is $A_\mu^a = \bar{q}\gamma_\mu\gamma_5\frac{\lambda^a}{2}q$.

Throughout this work we have expressed F in the chiral limit in terms of the physical pion decay constant F_π. The corresponding expression coincides with the one in $SU(3)$ χPT [25, 38], once resonance saturation of the $\mathcal{O}(p^4)$ χPT counterterms is assumed [44]. It reads

$$\begin{aligned} F_\pi &= F\left\{1+\frac{1}{16\pi^2F_\pi^2}\left[A_0(m_\pi^2)+\frac{1}{2}A_0(m_K^2)\right]\right. \\ &\left.+\left[\frac{4\widetilde{c}_d\,\widetilde{c}_m(m_\pi^2+2m_K^2)}{F_\pi^2M_{S_1}^2}-\frac{8c_d\,c_m\,(m_K^2-m_\pi^2)}{3F_\pi^2M_{S_8}^2}\right]\right\}. \end{aligned} \tag{C.2}$$

D Scattering amplitudes

By using crossing symmetry and isospin symmetry, as we discussed in Section 4, all the meson-meson scattering amplitudes with well defined isospin and angular momentum in $U(3)$ χPT can be reduced to the calculation of 16 independent processes.

Due to the much lengthy expressions of the one-loop $U(3)$ χPT scattering amplitudes, we only provide here the analytical expressions for the tree level results at leading order, denoted with the superscript (2). For the remaining parts, comprising the ones from the loops and resonance exchanges, one can download the Mathematica file from http://www.um.es/oller/u3FullAmp16.nb, that can also be provided by the authors under request.

1. $\pi^+\pi^-\to\pi^0\pi^0$

$$T^{(2)}_{\pi^+\pi^-\to\pi^0\pi^0} = \frac{s-m_\pi^2}{F_\pi^2}\,. \tag{D.1}$$

2. $K^+\pi^+\to K^+\pi^+$

$$T^{(2)}_{K^+\pi^+\to K^+\pi^+} = \frac{m_\pi^2+m_K^2-s}{2F_\pi^2}\,. \tag{D.2}$$

3. $K^+K^-\to K^0\bar{K}^0$

$$T^{(2)}_{K^+K^-\to K^0\bar{K}^0} = \frac{s+t-2m_K^2}{2F_\pi^2}\,. \tag{D.3}$$

4. $\pi^0\pi^0\to\eta\eta$

$$T^{(2)}_{\pi^0\pi^0\to\eta\eta} = \frac{m_\pi^2(c_\theta-\sqrt{2}s_\theta)^2}{3F_\pi^2}\,. \tag{D.4}$$

5. $\pi^0\pi^0\to\eta\eta'$

$$T^{(2)}_{\pi^0\pi^0\to\eta\eta'} = \frac{m_\pi^2(\sqrt{2}c_\theta^2-c_\theta s_\theta-\sqrt{2}s_\theta^2)}{3F_\pi^2}\,. \tag{D.5}$$

6. $\pi^0\pi^0 \to \eta'\eta'$

$$T^{(2)}_{\pi^0\pi^0\to\eta'\eta'} = \frac{m_\pi^2(\sqrt{2}c_\theta + s_\theta)^2}{3F_\pi^2}\,. \tag{D.6}$$

7. $K^0\bar{K}^0 \to \eta\eta$

$$T^{(2)}_{K^0\bar{K}^0\to\eta\eta} = \frac{c_\theta^2(9s - 6m_\eta^2 - 2m_\pi^2) + 4\sqrt{2}c_\theta s_\theta(2m_K^2 - m_\pi^2) + 8s_\theta^2 m_K^2}{12F_\pi^2}\,. \tag{D.7}$$

8. $K^0\bar{K}^0 \to \eta\eta'$

$$T^{(2)}_{K^0\bar{K}^0\to\eta\eta'} = \frac{2\sqrt{2}c_\theta^2(m_\pi^2 - 2m_K^2) - c_\theta s_\theta(3m_\eta^2 + 3m_{\eta'}^2 + 8m_K^2 + 2m_\pi^2 - 9s) + 2\sqrt{2}s_\theta^2(2m_K^2 - m_\pi^2)}{12F_\pi^2}\,. \tag{D.8}$$

9. $K^0\bar{K}^0 \to \eta'\eta'$

$$T^{(2)}_{K^0\bar{K}^0\to\eta'\eta'} = \frac{8c_\theta^2 m_K^2 - 4\sqrt{2}c_\theta s_\theta(2m_K^2 - m_\pi^2) + s_\theta^2(9s - 6m_{\eta'}^2 - 2m_\pi^2)}{12F_\pi^2}\,. \tag{D.9}$$

10. $\eta\eta \to \eta\eta$

$$T^{(2)}_{\eta\eta\to\eta\eta} = \frac{1}{9F_\pi^2}\Big[c_\theta^4(16m_K^2 - 7m_\pi^2) + 4\sqrt{2}c_\theta^3 s_\theta(8m_K^2 - 5m_\pi^2) + 12c_\theta^2 s_\theta^2(4m_K^2 - m_\pi^2) + 16\sqrt{2}c_\theta s_\theta^3(m_K^2 - m_\pi^2) + 2s_\theta^4(2m_K^2 + m_\pi^2)\Big]\,. \tag{D.10}$$

11. $\eta\eta \to \eta\eta'$

$$T^{(2)}_{\eta\eta\to\eta\eta'} = \frac{1}{9F_\pi^2}\Big[\sqrt{2}c_\theta^4(-8m_K^2 + 5m_\pi^2) - c_\theta^3 s_\theta(8m_K^2 + m_\pi^2) + 3\sqrt{2}c_\theta^2 s_\theta^2(4m_K^2 - m_\pi^2) + 4c_\theta s_\theta^3(5m_K^2 - 2m_\pi^2) + 4\sqrt{2}s_\theta^4(m_K^2 - m_\pi^2)\Big]\,. \tag{D.11}$$

12. $\eta\eta \to \eta'\eta'$

$$T^{(2)}_{\eta\eta\to\eta'\eta'} = \frac{(4m_K^2 - m_\pi^2)(2c_\theta^4 - 2\sqrt{2}c_\theta^3 s_\theta - 3c_\theta^2 s_\theta^2 + 2\sqrt{2}c_\theta s_\theta^3 + 2s_\theta^4)}{9F_\pi^2}\,. \tag{D.12}$$

13. $\eta\eta' \to \eta'\eta'$

$$T^{(2)}_{\eta\eta'\to\eta'\eta'} = \frac{1}{9F_\pi^2}\Big[4\sqrt{2}c_\theta^4(-m_K^2+m_\pi^2) + 4c_\theta^3 s_\theta(5m_K^2-2m_\pi^2) \\ +3\sqrt{2}c_\theta^2 s_\theta^2(-4m_K^2+m_\pi^2) - c_\theta s_\theta^3(8m_K^2+m_\pi^2) + \sqrt{2}s_\theta^4(8m_K^2-5m_\pi^2)\Big]\,. \tag{D.13}$$

14. $\eta'\eta' \to \eta'\eta'$

$$T^{(2)}_{\eta'\eta'\to\eta'\eta'} = \frac{1}{9F_\pi^2}\Big[2c_\theta^4(2m_K^2+m_\pi^2) - 16\sqrt{2}c_\theta^3 s_\theta(m_K^2-m_\pi^2) \\ +12\sqrt{2}c_\theta^2 s_\theta^2(4m_K^2-m_\pi^2) - 4\sqrt{2}c_\theta s_\theta^3(8m_K^2-5m_\pi^2) + s_\theta^4(16m_K^2-7m_\pi^2)\Big]\,. \tag{D.14}$$

15. $K^+\pi^0 \to K^+\eta$

$$T^{(2)}_{K^+\pi^0\to K^+\eta} = -\frac{c_\theta(-9t+3m_\eta^2+8m_K^2+m_\pi^2) + 2\sqrt{2}s_\theta(2m_K^2+m_\pi^2)}{12\sqrt{3}F_\pi^2}\,. \tag{D.15}$$

16. $K^+\pi^0 \to K^+\eta'$

$$T^{(2)}_{K^+\pi^0\to K^+\eta'} = \frac{2\sqrt{2}c_\theta(2m_K^2+m_\pi^2) - s_\theta(-9t+3m_{\eta'}^2+8m_K^2+m_\pi^2)}{12\sqrt{3}F_\pi^2}\,. \tag{D.16}$$

E Numerical inputs

In the numerical discussion, we take the average values for the masses of the charged and neutral pions and kaons. The values taken are summarized below in units of MeV:

$$\begin{aligned} &m_\pi = 137.3\,, \quad m_K = 495.6\,, \quad m_\eta = 547.9\,, \quad m_{\eta'} = 957.7\,, \\ &F_\pi = 92.4\,, \quad \mu = 770.0\,, \quad M_\phi = 1020.0, \quad M_\omega = 783.0\,. \end{aligned} \tag{E.17}$$

References

[1] K. Nakamura, *et al.*, (Particle Data Group), J. Phys. G 37 (2010) 075021.

[2] G. F. Chew, "S-matrix Theory of Strong Interactions", W. A. Benjamin, Inc., New York, 1961.

[3] A. D. Martin and T. D. Spearman, "Elementary Particle Theory", North-Holland Publishing Company, Amsterdam, 1970.

[4] R. J. Eden, P. V. Landshoff, D. I. Olive and J. C. Polkinghorne, "The Analytic S-Matrix", Cambridge University Press, Cambridge, 1966.

[5] T. N. Truong, Phys. Rev. Lett. **61** (1988) 2526.

[6] A. Dobado, M. J. Herrero and T. N. Truong, Phys. Lett. B **235** (1990) 134.

[7] A. Dobado and J. R. Peláez, Phys. Rev. **D56** (1997) 3057.

[8] J. Nieves, M. Pavón Valderrama and E. Ruiz Arriola, Phys. Rev. D **65** (2002) 036002.

[9] J. Oller and E. Oset, Nucl. Phys. **A620** (1997) 438; (E)−*ibid* A **652**(1999) 407.

[10] J. A. Oller and E. Oset, Phys. Rev. **D60** (1999) 074023.

[11] G. F. Chew, S. Mandelstam, Phys. Rev. **119** (1960) 467.

[12] M. Albaladejo and J. A. Oller, Phys. Rev. Lett. **101** (2008) 252002.

[13] Keigi Igi and Ken-ichi Hisaka, Phys. Rev. D **59** (1999) 034005.

[14] I. Caprini, G. Colangelo and H. Leutwyler, Phys. Rev. Lett. **96** (2006) 132001.

[15] S. Descotes-Genon and B. Moussallam, Eur. Phys. J. **C48** (2006) 553.

[16] R. Kaminski, J. R. Peláez and F. J. Ynduráin, Phys. Rev. D **77** (2008) 054015; R. García-Martín, R. Kamiski, J. R. Peláez, J. Ruiz de Elvira and F. J. Ynduráin, arXiv: 1102.2183.

[17] Z. Xiao and H. Q. Zheng, Nucl. Phys. **A695** (2001) 273.

[18] H. Q. Zheng, Z. Y. Zhou, G. Y. Qin, Z. Xiao, J. J. Wang and N. Wu, Nucl. Phys. **A733** (2004) 235.

[19] J. R. Peláez, Phys. Rev. Lett.**92** (2004) 102001; J. R. Peláez, Mod. Phys. Lett. **A19** (2004) 2879.

[20] J. R. Peláez and G. Rios, Phys. Rev. Lett.**97** (2006) 242002.

[21] Z. X. Sun, L. Y. Xiao, Z. Xiao and H. Q. Zheng, Mod. Phys. Lett. A **22** (2007) 711.

[22] L. Y. Xiao, Z.-H. Guo and H. Q. Zheng, Int. J. Mod. Phys. A **22** (2007) 4603.

[23] Z.-H. Guo, J. J. Sanz-Cillero and H.-Q. Zheng, JHEP **06** (2007) 030.

[24] J. Nieves and E. Ruiz Arriola, Phys. Rev. D **80** (2009) 045023.

[25] J. Gasser and H. Leutwyler, Ann. Phys. **158** (1984) 142; Nucl. Phys. B **250** (1985) 465.

[26] W. A. Bardeen, Phys. Rev. **184** (1969) 1848.

[27] K. Fujikawa, Phys. Rev. D **21** (1980) 2848.

[28] S. L. Adler and W. A. Bardeen, Phys. Rev. **182** (1969) 1517.

[29] G.'t Hooft, Phys. Rev. D **14** (1976) 3432; Phys. Rep. **142** (1986) 357.

[30] G.'t Hooft, Nucl. Phys. **B72** (1974) 461; E. Witten, Nucl. Phys. **B156** (1979) 269; S. Coleman and E. Witten, Phys. Rev. Lett. **45** (1980) 100; G. Veneziano, Phys. Lett. **B95** (1980) 90.

[31] P. Di Vecchia and G. Veneziano, Nucl. Phys. B **171** (1980) 253; C. Rosenzweig, J. Schechter and T. Trahem, Phys. Rev. D **21** (1980) 3388; E. Witten, Ann. Phys. **128** (1980) 363.

[32] N. Beisert and B. Borasoy, Nucl. Phys. **A705** (2002) 433.

[33] T. Becher and H. Leutwyler, Eur. Phys. J. **C9** (1999) 643.

[34] J. M. Alarcón, J. Martín Camalich, J. A. Oller and L. Alvarez-Ruso, to appear in Phys. Rev. C, arXiv:1102.1537.

[35] P. Herrera-Siklody, J. I. Latorre, P. Pascual and J. Taron, Nucl. Phys. **B497** (1997) 345.

[36] R. Kaiser and H. Leutwyler, Eur. Phys. J. **C17** (2000)623.

[37] P. Herrera-Siklody, J. I. Latorre, P. Pascual and J. Taron, Phys. Lett. **B419** (1998) 326.

[38] R. Kaiser and H. Leutwyler, Proceedings of "Nonperturbative Methods in Quantum Field Theory". Edited by A. W. Schrweiber, A. G. Williams and A. W. Thomas. World Scientific, Singapore, 1998.

[39] N. Beisert and B. Borasoy, Phys. ReV. **D67** (2003) 074007.

[40] Z. Y. Zhou and Z.Xiao, Phys. Rev. **D83** (2011) 014010.

[41] M. Jamin, J. A. Oller and A. Pich, Nucl. Phys. B **587** (2000) 331.

[42] B. Kubis and S. P. Schneider, Eur. Phys. J. C **62** (2009) 511.

[43] R. Escribano, P. Masjuan and J. J. Sanz-Cillero, arXiv:1011.5884 [hep-ph].

[44] G. Ecker, J. Gasser, A. Pich, E. de Rafael, Nucl. Phys. **B321** (1989) 311.

[45] G. Ecker, J. Gasser, H. Leutwyler, A. Pich, E. de Rafael, Phys. Lett. **B223** (1989) 425.

[46] S. R. Coleman, J. Wess and B. Zumino, Phys. Rev. **177** (1969) 2239; C. G. Callan, S. Coleman, J. Wess and B. Zumino, Phys. Rev. **177** (1969) 2247.

[47] V. Cirigliano, *et al.*, Nucl. Phys. **B753** (2006) 139.

[48] B. R. Martin, D. Morgan and G. Shaw, "Pion-Pion Interactions in Particle Physics", Academic Press Inc., New York, 1976.

[49] F. Guerrero and J. A. Oller, Nucl. Phys. B **537** (1999) 459; (E) J. A. Oller, Nucl. Phys. B **602** (2001) 641.

[50] J. A. Oller, E. Oset and J. R. Peláez, Phys. Rev. D **59** (1999) 074001; (E)-*ibid* **60** (1999) 074023; (E)-*ibid* **75** (2007) 099903.

[51] J. A. Oller, E. Oset and J. R. Peláez, Phys. Rev. Lett. **16** (1998) 3452.

[52] J. A. Oller and U. G. Meissner, Phys. Lett. B **500** (2001) 263.

[53] J. A. Oller, Phys. Lett. B **477** (2000) 187.

[54] A. Lacour, J. A. Oller and U.-G. Meißner, Ann. Phys. **326** (2011) 241.

[55] C. D. Frogratt and J. L. Petersen, Nucl. Phys. **B129** (1977) 89.

[56] J. R. Batley *et al.* (NA48/2 Collaboration), Eur. Phys. J. C **54** (2008) 411.

[57] W. Ochs, Thesis, University of Munich , 1974.

[58] B. Hyams, *et al.*, Nucl. Phys. **B64** (1973) 134; P. Estrabooks, *et al.*, AIP Conf. Proc. **13** (1973) 37; G. Grayer, *et al.*, *Proceedings of the 3rd Philadephia Conference on Experimental Meson Spectroscopy*, Philadephia, 1972 (American Institute of Physics, New York, 1972), p.5; S. D. Protopopescu and M. Alson-Garnjost, Phys. ReV. **D7** (1973) 1279.

[59] R. Kaminski, L. Lesniak and K. Rybicki, Z. Phys. **C74** (1997) 79.

[60] D. Cohen, *et al.*, Phys. ReV. **D22** (1980) 2595.

[61] A. D. Martin and E. N. Ozmutlu, Nucl. Phys. **B158** (1979) 520.

[62] A. Etkin *et al.*, Phys. Rev. **D25** (1982) 1786.

[63] A. Mercer, *et al.*, Nucl. Phys. **B32** (1971) 381.

[64] P. Estabrooks, *et al.*, Nucl. Phys. **B133** (1978) 490.

[65] H. H. Bingham, *et al.*, Nucl. Phys. **B41** (1972) 1.

[66] D. Aston, *et al.*, Nucl. Phys. **B296** (1988) 493.

[67] T. A. Armstrong, *et al.*, Z. Phys. **C25** (1984) 91.

[68] W. Hoogland, *et al.*, Nucl. Phys. **B126** (1977) 109.

[69] M. J. Losty, *et al.*, Nucl. Phys. **B69** (1974) 185.

[70] A. M. Bakker, *et al.*, Nucl. Phys. **B24** (1970) 211.

[71] Y. Cho, *et al.*, Phys. Lett. **B32** (1970) 409.

[72] D. Jido, J. A. Oller, E. Oset, A. Ramos and U.-G. Meißner, Nucl. Phys. A **725** (2003) 181.

[73] S. J. Lindenbaum and R. S. Longacre, Phys. Lett. **B274** (1992) 472.

[74] P. Estrabooks and A. D. Martin, Nucl. Phys. **B79** (1974) 301.

[75] Z. H. Guo, J. J. Sanz-Cillero, Phys. Rev. **D79** (2009) 096006.

[76] T. Feldmann, Int. J. Mod. Phys. **A15** (2000) 159.

[77] R. J. Eden and J. R. Taylor, Phys. ReV. **133** (1964) B1575.

[78] G. Mennessier, S. Narison and X.-G. Wang, Phys. Lett. B **688** (2010) 59.

[79] J. A. Oller, Nucl. Phys. A **727** (2003) 353.

[80] J. Weinstein and N. Isgur, Phys. Rev. Lett. **48** (1982) 659; Phys. Rev. D **27** (1983) 588; Phys. Rev. D **41** (1990) 2236.

[81] J. Weinstein,Phys. Rev. D **47** (1993) 911.

[82] G. Janssen, B. C. Pearce, K. Holinde and J. Speth, Phys. Rev. D **52** (1995) 2690.

[83] L. Alvarez-Ruso, J. A. Oller and J. M. Alarcón, Phys. Rev. D **80** (2009) 045011; *ibid* **82** (2010) 094028.

[84] S. Weinberg, Phys. Rev. D **11** (1975) 3583.

[85] S. Peris and E. de Rafael, Phys. Lett. **B348** (1995) 539.